ELECTRO-SORPTION OF SIMPLE ELECTROLYTES ONTO POROUS CARBON-BASED COMPOSITE ELECTRODES FROM WATER

by

Yu-Ching Kao

A thesis submitted to the Faculty of the University of Delaware in partial fulfillment of the requirements for the degree of Master of Civil Engineering

2020 Summer

ELECTRO-SORPTION OF SIMPLE ELECTROLYTES ONTO POROUS CARBON-BASED COMPOSITE ELECTRODES FROM WATER

by

Yu-Ching Kao

Approved: _____
Chin-Pao Huang, Ph.D.
Professor in charge of thesis on behalf of the Advisory Committee

Approved: _____
Jack A. Puleo, Ph.D.
Chair of the Department of Civil and Environmental Engineering

Approved: _____
Levi T. Thompson, Ph.D.
Dean of the College of Engineering

Approved: _____
Douglas J. Doren, Ph.D.
Interim Vice Provost for Graduate and Professional Education and
Dean of the Graduate College

ACKNOWLEDGMENTS

First, I would like to express my sincere gratitude to my advisor, Professor Chin-Pao Huang for his patient mentoring and guidance throughout not only my research work but also theses three years of my life as a graduate student.

I would like to thank all members in the aquatic chemistry laboratory: Dr. Ching-Lnug Chen (Tommy), Dr. Jenn-Feng Su, Dr. Rui-Mei Fan, Dr. Jui-Yen Lin, Jing-Hua Tzeng, Daniel Carreroto Sanchez, Muhsiang Hsieh, Dachuan Tang, Wanze Li, Michael Huang, Kegang Wei, and Cuijuan Feng for their assistance on my laboratory work. I would like to give special thanks to Tommy who has taught me all the things I need to learn in the laboratory and Jing-Hua who is the best partner in CDI group and always shared with me lots of precious experience.

I am grateful to Dr. Yu-Han and Mr. Michael Davidson for their professional help on my research and also being a warm friend with me at UD. I also want to thank my roommates, Hsuan-Lan Wang and Jialiu Jiang for taking good care of me and exploring life in the US with me. I could not get through all of tough things during my graduate study without their accompanying.

Last but not least, I would like to express my deepest gratitude to my parents and my family members who are always my strongest support during these years.

TABLE OF CONTENTS

LIST OF TABLES

LIST OF FIGURES

ABSTRACT

Capacitive deionization (CDI) is an emerging technology for the removal of charged ionic species from aqueous solution; also it has several merits like low cost and high energy efficiency. Electrodes made of commercial activated carbon with high specific surface area supported on graphite sheet (AC/G) were successfully fabricated and used to remove sodium chloride from dilute aqueous solution. A series of experiments on NaCl electro-sorption by NSA/G electrodes were run at different initial NaCl concentrations, applied potentials, and solution pH values. Direct measurement is found to be more accurate than indirect measurement of conductivity when assessing NaCl removal from aqueous solution. Langmuir and Freundlich isotherm models were used to describe sodium electro-sorption at different time periods (i.e., 80 min and 10 min). The electro-sorption and desorption of sodium on NSA/G electrodes followed the pseudo-first-order model in 1mM NaCl. Results showed applied voltage and pH were both important factors on sodium electro-sorption. The highest sodium adsorption of *ca.* 0.24 mmol/g in 1 mM NaCl occurred at $E\text{-}E_{pzc}$ = -1.0 V (vs. SCE) and pH_i = 10. The Gouy-Chapman theory can be adopted to preliminarily estimate the adsorbed sodium charge density in terms of potential and pH effects. The cyclic voltammetry results suggested that adsorption time was an important factor when predicting the sodium charge density in 1 mM NaCl through CV method. Moreover, a ratio around 0.3:1 of the sodium charge density estimated from CV to that measured from 10 min NaCl electro-sorption at the same applied potential was successfully derived, indicating the possibility of using CV for predicting ion removal capacity.

Chapter 1

INTRODUCTION

Due to the ever increasing agricultural, domestic, and industrial water demand, an energy efficient water extraction and treatment process methods is necessary in the future [1]. The fresh water accessible for humankind only occupies less than 0.5 % of global water resource, brackish water and seawater desalination is one of the crucial strategies for solving the water shortage problem [2]. Nowadays reverse osmosis (RO), multi-stage flash (MSF), multi-effect distillation (MED), and electrodialysis (ED) are the most widely applied desalination methods. However, the above technologies have some limitations such as high energy consumption, membrane fouling, and production of secondary wastewater which limit them to become a sustainable solution option. Capacitive deionization (CDI), having several merits such as high energy efficiency, environmental friendliness, robustness, and high ion removal performance, has emerged as a better suited alternative to existing desalination methods [3]. In addition to desalination, CDI can also integrate with RO system [4] and be utilized in water softening [5] ,which make it a widely applicable technology on various industrial processes.

In a typical CDI cell, a low DC voltage (about 1.2 V) is applied to the electrode made of porous carbon and a stream of untreated water is pumped into the cell during the charging process. Electrode materials and surface modification on the electrode have key influence on ion storage capacity. As the electrode is polarized, the excess charge formed on the electrode surface enhance the adsorption of counter ions within the double

layer (EDL) [6]. According to Stumm et al. (1970) [7] and Huang et al. (1976) [8], a polarizable interface and a reversible interface can establish in the EDL. Therefore, the charge density on the electrode side together with the capacitance of the electrode can be increased by adjusting the external applied electric field, i.e. a polarizable electrode and the concentration of potential determining species (pdi) such as H^+ and OH^-, i.e. a reversible electrode [9]. Until now, most CDI studies only focus on external electric field as the major source of surface charge on the electrode [10]. The electro-sorption process in the presence of an electrical flied at specific concentration of pdi (e.g. solution pH) is rarely investigated.

Additionally, assess of CDI performance is usually assuming symmetric adsorption on anion and cation in single salt solutions and measuring the conductivity of the effluent which lacks for the information of actual anion and cation adsorption density respectively [11]. Moreover, specific capacitance measurements through CV are mostly made in a high electrolyte concentration which seems inappropriate to CDI application because CDI is usually operated in a low concentration which is about two orders lower than that in CV [12]. Based on the above points, this work aims to study the electro-sorption of anions and cations separately and analyze the adsorption density for specific ions in terms of the effects of applied potential and solution pH. The concept of electrocapillarity and CV running in different electrolyte concentrations were applied to explore the relation between differential capacitance calculated from CV and the ion adsorption density obtained from direct electro-sorption processes.

The hypothesis for this study is by incorporating commercial F400 as a high pH_{pzc} activated carbon (AC) on the anode and commercial Nuchar SA as a low pH_{pzc} AC on the cathode will greatly enhance the anion and cation removal in a specific pH

range. Surface properties of the two commercial ACs were established. This work covers the part of investigating the characteristic adsorption of sodium and chloride ions by the Nuchar-SA/Graphite electrode with negatively-charged surface first. Results from this study provide a fundamental basis for understanding the predominant factors in electro-sorption processes and CV analysis in CDI which can be further applied to the electro-sorption by the F400/Graphite electrode in future studies before successfully combining the two different surface-charged electrodes into a complete CDI cell.

Chapter 2

THEORETICAL ASPECTS

2.1 Capacitive Deionization (CDI)

Capacitive deionization (CDI), also called electro-sorption, has emerged over years as an energy efficient and cost effective technique [13] for removing dissolved, charged species from aqueous solution [14] and desalination of water with a low or moderate salt content [15]. The energy efficiency of CDI for water with lower salt concentration is due to the fact that salt as the minority in the water are removed from the mixture while other methods extract water which is the majority phase from the salt solution. Furthermore, energy recovery is possible in CDI by utilizing the energy release during discharging step to charge another CDI cell [15].

A CDI cell is usually composed of a pair of oppositely-charged porous carbon electrodes with a separator in-between and can be assembled in stacks of multiple pairs. A CDI cycle consists of two steps, charging for water purification and discharging for cell regeneration. In the charging step, or ion electro-sorption step, the CDI pair is charged typically 1-1.4 V (called the cell voltage) and ions or charged species in the feed water migrate into the pores inside the carbon material and are immobilized within electrical double layers (EDLs). In the following discharging step, ions are released by reversing or shorting the cell voltage, creating a brine stream enriched in ions [15]. A cycle of the two steps of CDI operation is alternated to produce two streams of desalinated water and brine [1].

Comparing to the limited development of CDI in the past decades, CDI attracted enormous attention in recent years, including the development of membrane CDI (MCDI) [16][17], novel architectures for CDI cells like flow-through electrodes [18] and flow electrodes [19], hybrid CDI [20], inverted CDI [21], and optimized operational modes such as stop-flow operation during ion release [22], salt release at reversed voltage in MCDI [23], constant-current operation [24], and energy recovery from the discharging step [25].

CDI electrodes are mainly made of porous carbon materials possessing characteristics such as large specific surface area, suitable pore size and distribution, high electronic conductivity, good chemical and electrochemical stability over wide range of pH values, low hydraulic resistance, and large electrical double-layer capacitance of the electrode in order to enhance ion removal efficiency from electro-sorption processes [26]. A diverse of carbon materials were used for CDI electrodes including carbon aerogels and activated carbons as the most investigated materials [26], newer materials like activated carbon cloth [27], carbon felt [28], carbon black [29], carbon nanotubes [30], carbon nanofiber [31], graphene [32], reduced graphene oxide [33], and mesoporous carbon [34][35]. Activated carbon among the above materials is the most cost-effective materials with advantages of low cost, stability, well-balanced pore size distribution of mesopores and micropores, high specific surface area, and good reproducibility of its commercial product which make activated carbon a most suitable electrode material for CDI [36].

2.2 Electrical Double Layer

In order to investigate salt adsorption and charge storage within porous carbon particles, the concept of the electrical double layer is brought up for discussion.

Generally, electrical double layer (EDL) is composed of two layers with opposite polarity formed at the interface between electrode and electrolyte. That is, when a charged electrode is immersed in electrolytic solutions, it will repel the co-ions and attract counter-ions to its surface. The whole array of charged species and oriented dipoles at the electrode-solution interface is called the electrical double layer [37]. The earliest EDL model is proposed by Helmholtz [38]. He showed that all surface charge on the electrode side is directly charge-compensated by countercharge adsorbed to the surface in a condensed plane. However, the resulting constant differential capacitance independent from potential and concentration is not true in the real system [39]. Hence the Gouy-Chapman model modified the Helmholtz model by introducing a diffuse layer into the EDL.

The Gouy-Chapman describes the electric potential decreases exponentially away from the surface to the bulk fluid. By combining the Poisson-Boltzmann equation, the potential profile through the diffuse layer can be derived [39]:

$$\frac{\tanh\frac{ze\Psi_x}{4k_bT}}{\tanh\frac{ze\Psi_0}{4k_bT}} = e^{-\kappa x}\ ,\ \kappa = \sqrt{\left(\frac{2Iz^2e^2}{\varepsilon\varepsilon_o k_b T}\right)} \tag{2-1}$$

or can be written as

$$\ln\tanh\left(\frac{ze\Psi_x}{4k_bT}\right) = \ln\tanh\left(\frac{ze\Psi_o}{4k_bT}\right) - \kappa x$$

where k_b is the Boltzman constant, T (K) is the absolute temperature, ε is the dielectric constant of the medium, ε_0 is the permittivity of free space, e is the charge on the electron, and κ^{-1} (m) is the Debye length or the thickness of double-layer. In dilute aqueous solutions where $\varepsilon = 78.49$ and $\kappa = (3.29\text{x}10^9)zI^{1/2}$ (m^{-1}) at 25°C,

$$\ln\tanh(9.72\Psi_x) = \ln\tanh(9.72\Psi_0) - 3.29\times10^9 z\, x\sqrt{I} \quad (2\text{-}2)$$

where Ψ_x and Ψ_0 are the potential (V) at distance x (m) and at electrode surface, I (M) is the ionic strength of the solution, and z is the magnitude of the charge on the ions. By plotting $\sqrt{I}$ as a function of $\ln\tanh(9.72\Psi_x)$, Ψ_0 can be determined. If Ψ_0 is sufficiently low that $\Psi_0 \leq 50/z\ (mV)\ at\ 25$ ℃, eq. (2-2) can be simplified as

$$\Psi_x = \Psi_0 e^{-\kappa x} \quad (2\text{-}3)$$

$$\Psi_0 = e \times \Psi_x \quad \text{when } x = \kappa^{-1} \quad (2\text{-}4)$$

Furthermore, by considering a Gaussian box at the electrode-solution interface, the relation between surface charge and surface potential can be obtained [39]:

$$\sigma^M = -\sigma^S = \sqrt{8k_bT\varepsilon\varepsilon_0 I}\sinh(\frac{ze\Psi_0}{2k_bT}) \quad (2\text{-}5)$$

For dilute aqueous solutions (ε=78.49) at 25°C, the constants can be evaluated to give

$$\sigma^M = -\sigma^S = 0.117\sqrt{I}\sinh(19.5z\Psi_0) \quad (2\text{-}6)$$

where σ^M and σ^S are the surface charge (C/m^2) on the electrode side and solution side, Ψ_0 (V) is the potential at electrode surface relative to the bulk solution, I (M) is the ionic strength of the bulk solution, and z is the magnitude of the charge on the ions.

Combining the two models mentioned above, in Stern's model, EDL is consisted of a compact layer adhere to the electrode known as Stern layer or Helmholtz layer and the diffuse layer shown in Fig. 2.1 (a). The Stern's model accounts for ions with finite size and a layer of solvent on the electrode surface. Therefore, the compact layer can be separated into the inner Helmholtz plane (IHP) where specifically adsorbed ions and solvent molecules are and the outer Helmholtz plane (OHP) where the nearest solvated

ions are. And those nonspecifically adsorbed ions are distributed in the diffuse layer beyond the OHP [39]. The total excess charge density on the solution side can be given as the sum of the excess charge density from specifically adsorbed ions in IHP, σ^i, and the excess charge density in the diffuse layer, σ^d:

$$\sigma^S = \sigma^i + \sigma^d = -\sigma^M \tag{2-7}$$

Moreover, the total differential capacitance, C, in the Stern's model can be subdivided into two parts being connected in series, that is, the capacitance in the outer Helmholtz plane (or Stern's layer), C_H, and the capacitance in the diffuse layer, C_D, expressed in the form of reciprocals and in Fig. 2.1 (b):

$$\frac{1}{C} = \frac{1}{C_H} + \frac{1}{C_D} \tag{2-8}$$

At low ionic strength, potential at Helmholtz plane is large, thus $\frac{1}{C_D} > \frac{1}{C_H}$ [7] . We assume Stern' layer can be ignored in our study, so the EDL built in the electrode-solution interface is treated as only composed of the diffuse layer. Hence the potential distribution and charge storage in the EDL are predicted by applying the Gouy-Chapman model in later chapters.

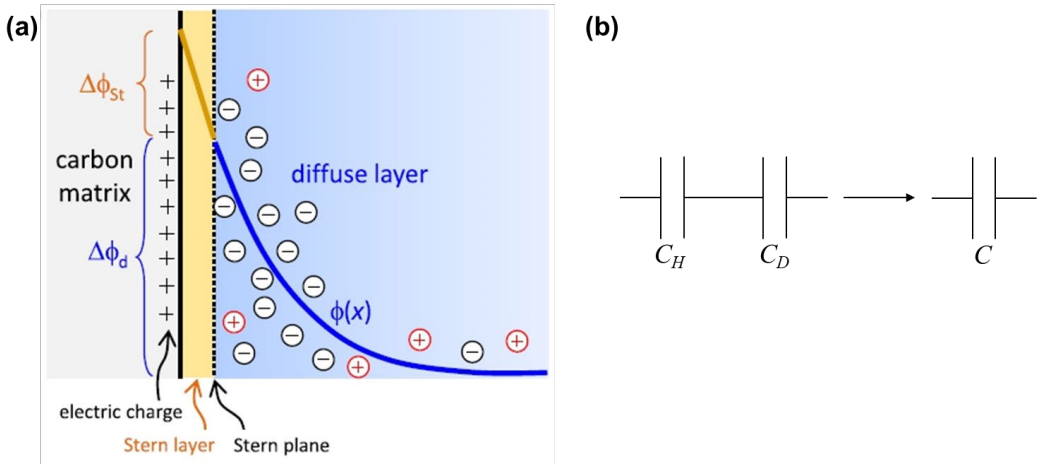

Figure 2.1 (a) Structure of the electrical double layer and (b) equivalent circuit of the total capacitance according to the Stern's model [15][7]

2.3 Electrocapillarity

An ideal polarizable electrode is like an electrical condenser without leakage [37]. This means that no charged species (including electrons) across the interface. A polarizable electrode-electrolyte interface is formed where a potential difference across the EDL is applied from an external power source. And the potential difference is that between the polarized electrode and the reference electrode. Besides, the capacitance of polarized electrode alters when charges approach or leave the interface [7].

The electrocapillary curves are the experimental data showing the interfacial tension of mercury in an ideal polarized electrode varies with the applied potential across the interface [37]. According to the thermodynamic theory of electro-capillarity, for an ideal polarized electrode, the slope of the electro-capillary curves, namely the differentiate of the surface tension is equal to the excess charge density on the metallic electrode (known as First Lippmann Equation [7][40][41]):

$$\left(\frac{\partial \gamma}{\partial \mathrm{E}}\right)_{\mu,T,P} = -\sigma_E^M \tag{2-9}$$

where γ is the surface tension in the electro-capillary curve (dyn/cm), E is the polarizable potential (V), and σ_E^M is the charge density (C/m^2) on the electrode side. Based on the definition of differential capacitance:

$$\mathrm{C} = \frac{\mathrm{d}\sigma_E^M}{\mathrm{dE}} \tag{2-10}$$

the differential capacitance C_E (F/g or F/cm^2) contributed from a polarizable electrode can be predicted by differentiating eq. (2-9) shown in the following equation (known as Second Lippmann Equation [7]) [42]:

$$\left(\frac{\partial^2 \gamma}{\partial \mathrm{E}^2}\right)_{\mu,T,P} = -\left(\frac{\partial \sigma_E^M}{\partial E}\right)_{\mu,T,P} = C_E \tag{2-11}$$

The differential capacitance of the interface characterizes the electrode's ability to store charge in response to a change in potential. In other words, the differential capacitance of a polarizable electrode, C_E, is not constant with potential like an ideal capacitor [39].

The three important variables, surface tension, charge, and capacitance, as a function of potential in electro-capillary theory are show in Fig. 2.2 (a). The electrocapillary curves provide information on the specific adsorption of dissolved substances on the electrode. As shown in Fig. 2.2 (a), at E_{pzc} (namely electrocapillarity maximum, ECM), the differential capacitance is at its minimum. This is also the potential of zero charge (E_{pzc}) where $\sigma_E^M = 0$ [7]. By simply following the principle that differential capacitance is the first differentiate of charge density, charge density can be determined by integrating the differential capacitance. And since capacitance is the second differentiate of surface tension, surface tension can be calculated by second integral of the differential capacitance derived from CV curves. In that way, CV measurement may be a feasible way to estimate ion adsorption by the electrode used.

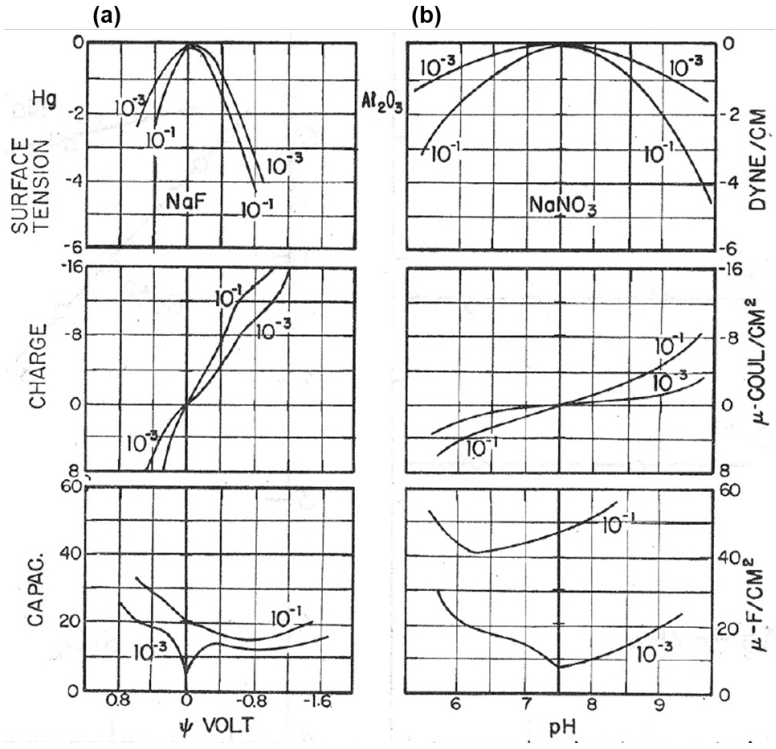

Figure 2.2: Comparison between (a) the polarized electrode-electrolyte and (b) the reversible oxide-electrolyte interface [7]

2.4 Reversible vs. Polarizable Electrodes

Two classes of interfaces are comprised of the electrical double layer. One is the polarizable interface described in Electrocpillarity in section 2.3 and the other is the reversible interface [8]. The major difference between two interfaces is the way in which the potential difference across the interface is established [7]. Unlike from the external applied potential, for a reversible interface, the potential at the electrode-solution interface, Ψ_0 (V), is determined when the electrode surface with multi-functional groups is in equilibrium with the potential determining species in the solution [7]. In this context, it is assumed that H^+ and OH^- are the sole potential determining species. Thus Ψ_0 (V) is associated with the concentration of H^+ and OH^-, which is the pH value of the solution.

By employing the zeta potential data measured for the electrode and eq. (2-2) from the Gouy-Chapman theory, the potential at the electrode-solution interface, Ψ_0 (V), can be easily calculated.

By further applying the relation of charge density and the potential created on the surface from eq. (2-6), charge density on the reversible interface can be derived:

$$\sigma_{pH}^{M} = 0.117\sqrt{I}\sinh(19.5z\Psi_0) \tag{2-12}$$

or can be written as:

$$\Psi_0 = \frac{1}{19.5}\sinh^{-1}\left(\frac{\sigma_{pH}^{M}}{0.117\sqrt{I}}\right) \tag{2-13}$$

where σ_{pH}^{M} is the surface charge (C/m^2) on the electrode side, Ψ_0 (V) is the potential at electrode surface relative to the bulk solution.

At the point of zero charge (pH_{pzc}), Ψ_0 is equal to zero implying no excess positive or negative charge on the surface. We may not always know the absolute value of Ψ_0. However, a potential difference exists when the bulk concentration of potential determining species differs from pH_{pzc} and it can be expressed from the Nernst equation [42]:

$$d\Psi_0 = -0.05913\ dpH \tag{2-14}$$

Along with eq. (2-14) and based on the definition of the differential capacitance, the differential capacitance of a reversible electrode, C_{pH}, can be acquired [8][6]:

$$C_{pH} = -\frac{d\sigma_{pH}^{M}}{d\Psi_0} = -\frac{d\sigma_{pH}^{M}}{dpH}\frac{dpH}{d\Psi_0} = 16.9\frac{d\sigma_{pH}^{M}}{dpH} \tag{2-15}$$

Because the electrical double layer is composed of two kinds of interfaces, the total differential capacitance of an electrode is the combination of differential capacitances derived from the polarizable electrode (C_E) and from the reversible electrode (C_{pH}). According to eq. (2-11) and eq. (2-15) obtained above, the total differential capacitance, C, can be expressed as [6]:

$$\mathrm{C} = -\frac{d\sigma^M}{dE} = -\left(\frac{d\sigma_E^M}{dE} + \frac{d\sigma_{pH}^M}{dE}\right) = -\frac{d\sigma_E^M}{dE} + 16.9\frac{d\sigma_{pH}^M}{dpH} = C_E + C_{pH} \qquad (2\text{-}15)$$

Fig. 2.3 shows the two capacitors, one of polarizable (C_E) and the other of reversible (C_{pH}) are connected in parallel, indicating not only the external applied potential but also the functional groups resulted from potential determining species on the electrode surface will contribute to total capacitance. Consequently, this work studied the effects of applied potential and solution pH on the electro-sorption experiments in NaCl solution which will be explained in chapter 4.

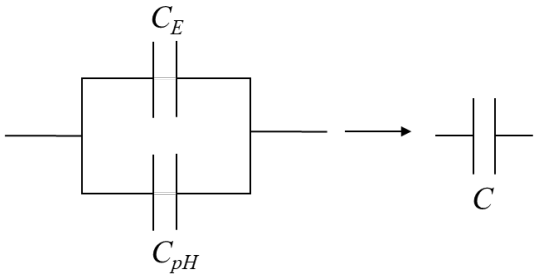

Figure 2.3: Equivalent circuit of the total capacitance of the electrical double layer

Chapter 3

MATERIALS AND METHODS

3.1 Materials

The two activated carbon (AC) materials used in this study were both commercially available: Filtrasorb 400 (Calgon Carbon Co., Moon Township, PA, USA) and Nuchar-SA (Westvaco Co., Covington, VA, USA). These two materials will be referred to as F400 and NSA, respectively. The graphite sheet (sheet thickness = 3 mm, area = 30 x 30 cm^2 per sheet), purchased from GraphiteStore.com, Inc. (Northbrook, IL, USA) was cut and used as the substrate to immobilize the activated carbon materials.

All solutions were prepared from Fisher Reagent Grade chemicals (Fisher Scientific, Fair Lawn, NJ, USA) and deionized water. Sodium chloride (NaCl) was dissolved into deionized water to prepare stock solution. Sodium hydroxide (NaOH) and hydrochloric acid (HCl, 36.5-38%) were used to adjust solution pH to specific values. A Fisher Model Accumet AE150 pH (Fisher Scientific, Fair Lawn, NJ, USA) meter was used for the pH measurements. Chemicals used in ion chromatography analysis were: sodium carbonate (Na_2CO_3), sodium bicarbonate ($NaHCO_3$), nitric acid (HNO_3, 69.5wt%), and dipicolinic acid (0.02 M $C_7H_5NO_4$ in water) obtained from Sigma-Aldrich (St. Louis, MO, USA).

3.2 Experimental Procedures

3.2.1 Preparation of AC electrodes

Prior to making the AC slurry, granular F400 AC was ground into F400 powder and sieved through ASTM sieve # 200, while powdered NSA AC without grinding was sieved through ASTM sieve # 325 directly. Notably, both AC materials were not washed by DI water or acid-base solutions after sieving in order to avoid any change on their surface functional groups. Both F400 and NSA electrodes were made by the same procedure. The AC slurry was prepared by mixing N-Methyl-2-pyrrolidone (NMP, 98% Fisher Scientific, Fair Lawn, NJ, USA) as the solvent and Polyvinylidene fluoride (PVDF, M.W.=530,000, Sigma-Aldrich) as the binder into homogeneous solution with a 30:1 NMP: PVDF weight ratio. Then AC material was added into the solution with a 4: 1 AC: PVDF weight ratio. The mixture with total weight of 7 g was stirred overnight to obtain homogeneous AC slurry.

A bare graphite sheet with the size of 5 x 12 cm^2 was scraped by sand paper for about 50 times in the same direction to create a rougher surface. The graphite sheet was later washed by DI water in ultrasonic tank for 3 min and dry in the furnace in air at 105 $^{\circ}C$ for 2 h. Then the AC electrode was made by casting the AC slurry uniformly onto a limited area (5 x 8 cm^2) of the graphite sheet, denoted as AC/G. The wet AC/G was then sent into furnace and heated at 210 $^{\circ}C$ for 1 h to have all NMP solvents evaporated and solidify the binder. Finally, each AC/G electrode will include an effective area of 40 cm^2 with total AC weight of 0.8 g on it. Before any experiment, AC/G was immersed in deionized water overnight and then vibrated in an ultrasonic tank (Fisher Model FS-20, 40 kHz) for 3 min to ensure that proper wetting conditions were maintained and no air bubbles were trapped in the porous material.

3.2.2 Electro-sorption Experiments

Three-electrode system was used in all electrochemical experiments in order to obtain comparable applied potentials on the working electrode. As the AC/G being the working electrode (WE), a bare graphite sheet with a geometric area around 5 x 8 cm^2 was used as the counter electrode (CE). The working electrode and the counter electrode were positioned in parallel at an average distance of 2 cm and a reference electrode of Hg/Hg_2Cl_2/4M KCl (E° = 0.241V vs. NHE) (RREF0022, Pine Instrument Inc., Grove City, PA, USA) was placed in the middle with the tip close to the working electrode. Fig. 3.1 shows the electrochemical cell used to conduct electro-sorption experiments controlled by a potentiostat (Pine Biopotentiostat model AFRDE 4, Pine Instrument Inc., Grove City, PA, USA) at room temperature. The current signal was recorded through the Dataq voltage data logger (DI-808, Dataq Instruments Inc., Akron, Ohio, USA). This setup was also used in CV measurements.

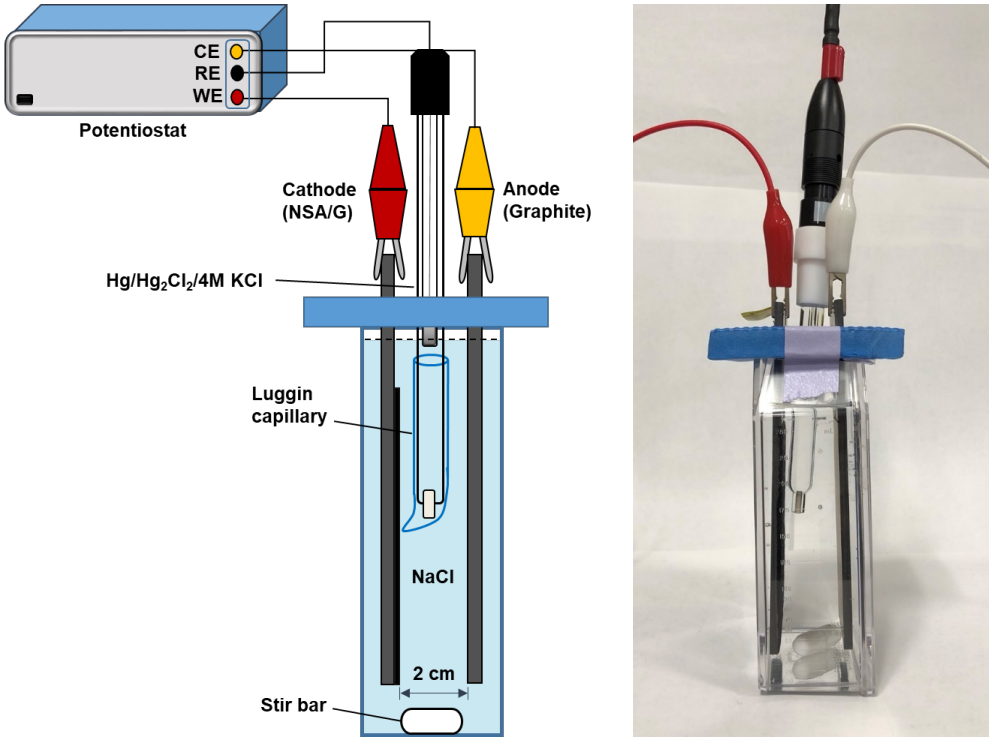

Figure 3.1: Design of electrochemical cell used to conduct batch electro-sorption experiments and CV measurements (side view)

Indirect measurement-conductivity

Commonly, a conductivity meter is attached to the CDI system in order to monitor the conductivity variation continuously at the outlet of the CDI cell. The relationship between solution conductivity and NaCl concentration is obtained according to the calibration table made prior to the experiment. In this study, the initial and final conductivity of the reacting NaCl solution from batch electro-sorption experiments mentioned above were also measured by a conductivity meter (Oakton, CTSTestr™ 50P, Vernon Hills, IL, USA) for comparison with the literature data.

In addition, the ideal electrolytic conductivity can be calculated theoretically by the following equations according to the definition [39]:

$$\mu = z_+ \nu_+ \lambda_+ + z_- \nu_- \lambda_- \quad (3\text{-}1)$$

$$\lambda_T = \Sigma C_i \mu_i = C_i z_+ \nu_+ \lambda_+ + C_i z_- \nu_- \lambda_- \quad (3\text{-}2)$$

where C_i is the concentration of electrolyte i (mol/1000 cm^3), μ is the molar conductivity (S-cm^2/mol), λ is the equivalent ionic conductivity (S-cm^2/equiv), λ_T is the total conductivity (S-cm^{-1}), z is the magnitude of the charge on the ions, and ν is the number of anions and cations per formula unit of electrolyte respectively.

Direct measurement

Batch-mode adsorption-desorption experiments of CDI cell were conducted in different concentrations of 250 ml NaCl solutions under neutral pH (pH 6.5) at -0.3V (vs. SCE) for 80 min at room temperature. The experiments were then followed by a desorption process by reversing the applied potential (+0.3V vs. SCE) for 80 min in the same condition. After one cycle of adsorption and desorption, both working and counter electrodes will be placed into DI water in separate beakers to desorb remaining ions on the electrodes by applying ±1V (vs. SCE) to the electrodes. An ion chromatography (IC) was used to analyze the concentration of individual species (Na^+ and Cl^-) in the solution during the electro-sorption experiments, that is, the direct measurement. After the electro-sorption experiments under a certain pH value and applied voltage were done, experiments under different pH values (pH 3 and pH 10) with different applied voltages (from -0.7V to +0.7V vs. SCE) were also conducted at room temperature to see how those parameters influence the performance of electro-sorption. Nitrogen gas was

purged into NaCl solution during the experiments only under pH 10 condition to prevent CO_2 dissolving into the solution rapidly.

3.2.3 Capacitance Measurement

In order to use Cyclic Voltammetry (CV) as a method to predict ion adsorption density in the batch electro-sorption experiments mentioned above, CV experiments were conducted in 250 ml NaCl solution under different concentrations and scan rates with the same experimental set-up as in the electro-sorption experiments. Starting initially from 0 V and within the scanning range of -0.9 V to +0.9 V (vs. SCE) for NSA/G as WE. The scanning ranges were decided where few faradic reactions happened. Besides, there are two main methods used to calculate the capacitance through CV measurements and demonstrated below.

Method 1 (Area method)

Most CDI studies calculated specific capacitance of the electrode by integrating the full CV cycle (to gain area between the CV curve) according to the following equation [43][44]:

$$\mathrm{C} = \frac{\oint I\, dV}{2m\nu\Delta V} \tag{3-3}$$

where C (F/g) is the specific capacitance, I (A) is the response current, V (V) is the potential, m (g) is the mass of activated carbon material, ν (V/s) is the scan rate, and ΔV (= V_a - V_c) is the potential window of CV as shown in Fig. 3.2. Since capacitance, C, is generally a function of potential, the specific capacitance obtained from method 1 is an average value of capacitance, that is “average C”, over the potential range of CV according to Bard [39].

Method 2 (Point method)

The current data derived from voltammetry experiments in this study can also be used in calculating the instantaneous capacitance, C (F g^{-1} or F cm^{-2}) as a function of E based on the theory of electrocapillarity [37]:

$$C \equiv \frac{d\sigma}{dE} = \frac{Idt}{dE} = \frac{I}{v} \tag{3-4}$$

$$C_a = \frac{I_a}{v} \tag{3-5}$$

$$C_c = \frac{I_c}{v} \tag{3-6}$$

where σ is the surface charge density (C/m^2), E is the polarizable potential (V), I is the current response (A), and v is the scan rate (V s^{-1}). The current in CV curve is composed of anodic current (I_a) and cathodic current (I_c), where I_c is opposite in sign to I_a which can be seen in Fig. 3.2. To compare the absolute values of I_a to I_c, I_c was added a negative sign and the curve of I_c was flipped along the x-axis in CV. Then both I_a and the flipped I_c were directly divided by the scan rate applied in CV measurements to obtain the values of instantaneous capacitance from negative (C_a) and positive (C_c) sweeps, respectively, which are later shown in Fig. 4.19 and 4.21. According to the electro-capillary theory mentioned in section 2.3, the charge density and the surface tension of an interface can be calculated by the integral of the instantaneous capacitance derived from CV curves.

In conclusion, though area method is the most generally used method to estimate specific capacitance of the electrode, it only calculates the average value of capacitance over a certain potential range. Instantaneous capacitance, on the contrary, reveals different values as a function of potential. Therefore, by exploiting point method with a

known capacitance, we can predict the voltage needed to applied in electro-sorption when designing experiments. In addition, by comparing the calculated charge density of adsorbed ions from the integral of instantaneous capacitance in CV with the actual ion adsorption density from direct batch electro-sorption experiments under the same experimental conditions, we can assess how reasonable CV can predict ion adsorption density in the electro-sorption process.

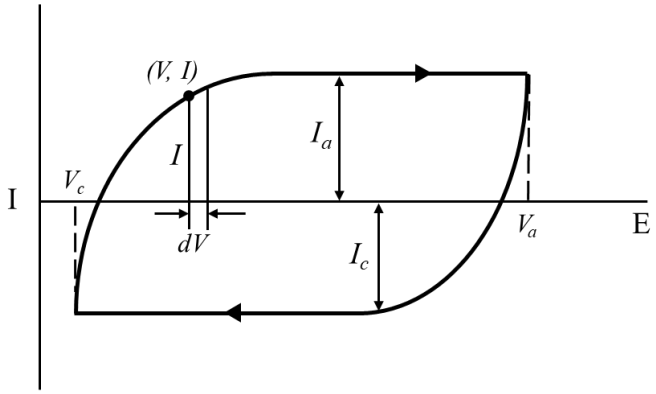

Figure 3.2: Current-potential plot resulting from a cyclic linear potential sweep (CV)

3.3 Chemical Analysis

In order to analyze individual species in the solution, the Metrohm ion chromatography (940 Professional IC, Metrohm, Riverview, FL, USA) system equipped with an auto-sampler and analytical columns (both anion and cation) was used to detect the concentration of sodium and chloride in this study. Before injecting the samples into IC, 1ml solution aliquots were withdrawn, diluted to 5ml and then filtrated through a 0.45-μm Nylon syringe filter (Simsii, Inc 133 Port Irvine, CA, USA). The mixture of 3.2 mM Na_2CO_3 and 1mM $NaHCO_3$ was used as anion eluent and the mixture of 1.7 mM HNO_3 and 0.7 mM dipicolinic acid ($C_7H_5NO_4$) as cation eluent for the effluent mobile phase in IC. 0.1 wt % methanol was used for suppressor rinse and 0.1 M H_2SO_4 as suppressor regenerant. A computer with MagIC Net software (version 2.4) was utilized for instrument operation and data processing. Both anion and cation pumps were degassing manually by removing the caps and drain eluent out the pipelines for 5 to 10 min before analysis. The Homework mode was run for about 20 min to ensure a stable baseline of conductivity value. All samples were injected by an auto-sampler connected to the IC. The injected samples would split into two flows and went through anion and cation columns separately. The flow rate was set at 0.7 ml/min for anion analysis and 0.2 ml/min for cation analysis. The injection volume was 20 μL for anion and 10 μL for cation. The total analysis time for each sample was 12 min.

3.4 Surface Characterization

The surface of activated carbon is characterized for specific surface area, pore size distribution, surface morphology, XPS, XRD, and surface charge. Before the measurements of BET, XPS, XRD, and zeta potential, F400 and NSA were processed into powder less than 75 μm and 45 μm, respectively, as mentioned in section 3.2.1. The surface area and pore size distribution of AC were deduced from the nitrogen physical adsorption measurement data obtained by using an accelerated surface area and porosimerty system (ASAP 2020, Micromeritics Instrument Corp., Norcross, GA, USA) based on the Brunauer–Emmett–Teller (BET) method. Before the measurement, powdered AC samples (each >100 mg) were stored in a freeze dryer and outgassed overnight under vacuum conditions at 10^{-6} Torr to remove moisture.

The micro-morphology and surface structure of AC coated on the electrodes were characterized by a scanning electron microscopy (SEM, Auriga 60, Carl Zeiss Co., Germany) with a resolution of 1 nm when operating at 15 kV acceleration voltage. The AC electrode samples were prepared in the size of 0.5 x 0.5 cm^2 and coated with a layer of gold for 90 seconds to prevent charging issue before SEM analysis. An energy-dispersed analysis of X-ray (EDX) apparatus was installed onto SEM to detect the elements composition on the electrode surface.

An X-ray photoelectron spectroscopy (XPS, K-Alpha XPS, Thermo Fisher Scientific Inc., USA) with an excitation source of monochromatic Al-Kα was utilized to analyze the surface chemistry of NSA and F400 activated carbons. Prior to transferring AC samples from a separate introducing chamber into the analyzer chamber, the samples were passed through a desorption chamber maintained at about 10^{-9} Torr in order to remove volatile matters. The C-C bond located at 284.8 eV was used as a reference peak for calibration when fitting the resulting spectra. An X-ray Diffraction

(XRD, Bruker D8, BRUKER AXS, Inc., Madison, WI, USA) with Cu-Kα radiation (40 kV, 40 mA) as the X-ray source was employed to deduce crystalline structure of the AC samples. The scanning degree (2θ) started from 10° to 90° with the increment of 0.05°/sec.

The surface charge of AC was measured in terms of zeta potential by using the Zetasizer (Malvern Nano ZS, Malvern Panalytical Ltd., UK). Both F400 and NSA powdered samples were not washed and 1g of AC powder was dispensed in 500 ml NaCl solution of various ionic strengths from 10^{-2} to10^{-1} M. 40 ml aliquots withdrawn from the AC suspension were collected in 24 centrifuge tubes for each ionic strength. To adjust the pH of AC dispersed NaCl solutions, different amount of HCl and NaOH were added to the solutions manually. Lastly, the adjusted NaCl solutions with AC powder were equilibrated in a reciprocal shaker overnight (about 24 h). And about 10 to 13 tubes with solution pH values from 1 to 12 were chosen and put into quartz cells for zeta potential measurements.

Chapter 4

RESULTS AND DISCUSSION

4.1 Characterization of Activated carbon

4.1.1 Surface Area and Pore Size

Brunauer–Emmett–Teller (BET) was performed to characterize the surface area and pore size distribution of the two activated carbons used in this study. Table 4.1 shows that both activated carbons have large surface area which are close to the reported numbers from other studies [9][45]. In addition, NSA AC contains average pore size around 7.3 nm and total pore volume around 1.2 cm^3/g. NSA also has a higher surface area than F400 does which may due to several reasons during the activation step like activation temperature and activating agents used, etc. [46] To sum up, large surface area of both AC is beneficial when being made into porous AC electrodes in electro-sorption applications.

Table 4.1: Surface area and pore size of NSA AC and F400 AC

AC	BET Surface Area (m^2/g)	Total Pore Volume (cm^3/g)	Average Pore Size (nm)
NSA	1732.63	1.16	7.26
F400	802.36	0.84[a]	15[a]

[a] From reference [47]

4.1.2 SEM Analysis

Scanning electron microscopy (SEM) was used to investigate the surface morphology of the graphite substrate and the prepared activated carbon electrodes. Fig. 4.1 (a), (c), and (e) illustrate larger rectangular particles with some scrapes on the graphite substrate and smaller irregular particles on both AC electrodes covering the graphite structure. It can be seen in a much closer magnification the parallel layer structure on the graphite substrate shown in Fig. 4.1 (b). Because micropores and macropores are very small and hard to be detected in SEM, only macropores and larger cavities showed in Fig. 4.1 (d) and (f) for NSA/G and F400/G electrodes. The parallel layer structure of graphite cannot be observed again when the activated carbons are coated on it.

Fig. 4.2 presents the SEM-EDX spectrum images of graphite substrate and the AC electrodes revealing the constituents of elements in weight percentage on the surface. It shows a 99.9% of C on graphite substrate indicating graphite composed of almost pure C. Both AC electrodes contain nearly 20 % of F which should come from the PVDF used in making the electrodes. If adding the other two major elements, C and O in activated carbon, about 80 % of C+O could be obtained in both NSA/G and F400/G. The ratio of (C+O): F correspond to the ratio of AC: PVDF for the preparation of AC electrodes in previous chapter. Other elements like P on NSA/G electrode and Al, Si, Fe, and Ca on F400/G electrode should result from the ash contents on AC due to lack of the washing step [9].

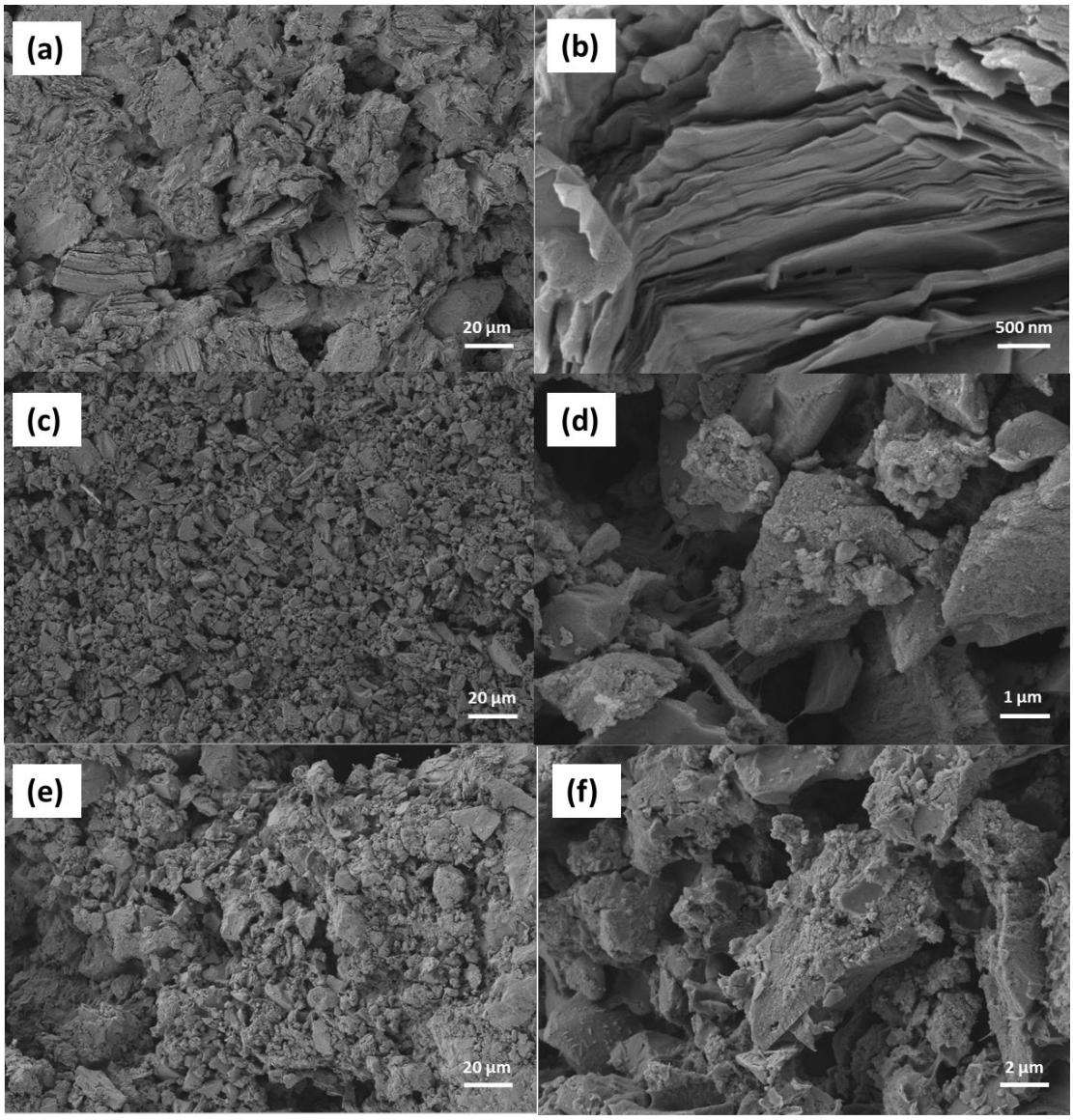

Figure 4.1: SEM observation of (a) & (b) graphite, (c) & (d) NSA/G electrode, and (e) & (f) F400/G electrode

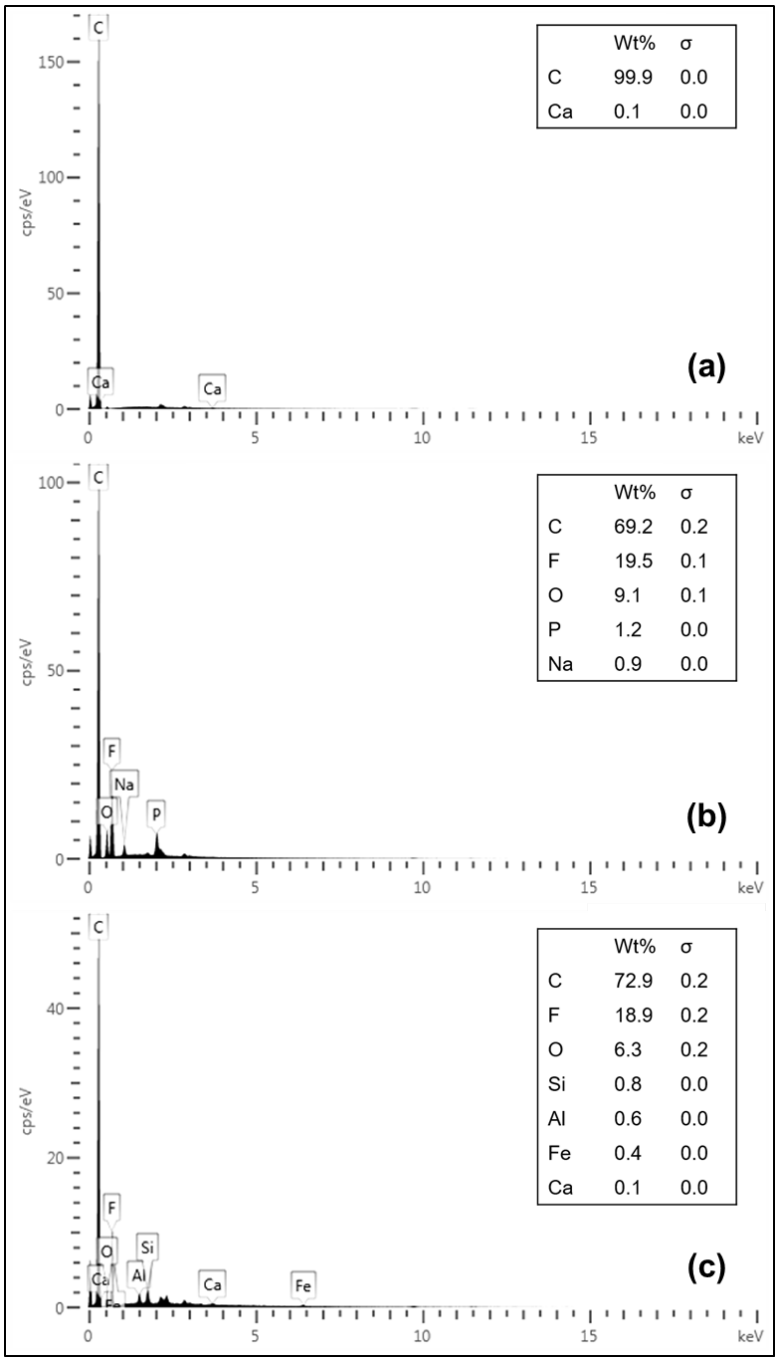

Figure 4.2: SEM-EDX spectrum image of (a) graphite, (b) NSA/G electrode, (c) F400/G electrode XRD analysis

Fig. 4.3 shows the crystal structure analyzed by X-ray Diffraction for Graphite, NSA and F400 activated carbons. The crystalline peaks showing in 2θ= 26.3°, 42.6°, 44.8°, 54.2°, and 77.5° for graphite sheet corresponding to the reflection planes (0 0 2), (1 0 0), (1 0 1), (0 0 4), and (1 1 0) can be assigned to C crystal as the form of graphite by referring to ICDD database. On the other hand, there was no crystal structure found in NSA AC and F400 AC. Only broad peaks near 25° and 40° appear which correspond to (0 0 2) and (1 0 0) reflections of disordered micro-graphitic stacking. This demonstrates that NSA and F400 ACs are less-crystalline porous solids with random orientation of the stacking units [48].

4.1.3 XPS Analysis

X-ray photoelectron spectroscopy (XPS) was used to determine the chemical state of elements found on the surface. Fig. 4.4 shows the XPS analysis of NSA and F400 activated carbons in terms of C 1s and O 1s atomic orbitals. Both activated carbons have C 1s peak deconvoluted into four peaks, C—C/C—H (aromatic C and protonated C at 284.8 eV), C—O (aromatic C at 286.1-286.6 eV), C=O (ketonic C at 286.8-288.3 eV), and COO (carboxylic C at 290.6-291.1 eV) [49]. Results show that aromatic and protonated compounds were the major C groups in NSA AC while F400 AC had higher percentage of C—O and carboxylic groups comparing to the aromatic groups. The XPS spectrum of O 1s for both AC shows three intense peaks at binding energy of 533.6-533.9, 531.2, and 532.4-532.6 eV corresponding to ether oxygen atoms in esters and anhydrides (R—O—C=O), carbonyl oxygen atoms in amides and anhydrides (O=C), and the carbonyl oxygen atoms in esters (O=C—O), respectively [50]. It is seen that NSA AC contains O—C and O=C as major O groups and F400 has the highest ratio of

O=C—O group. The groups of O=C and O=C—O were mainly contributed to the formation of oxygen-containing aromatic functional groups during activation [6].

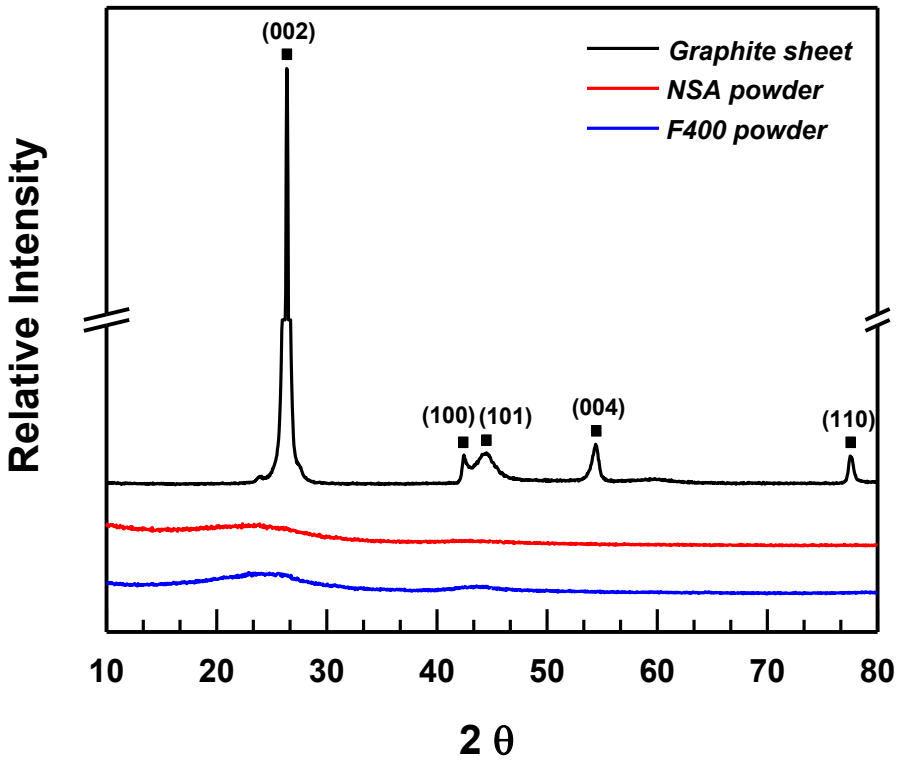

Figure 4.3: XRD spectrum of graphite, NSA and F400 activated carbons

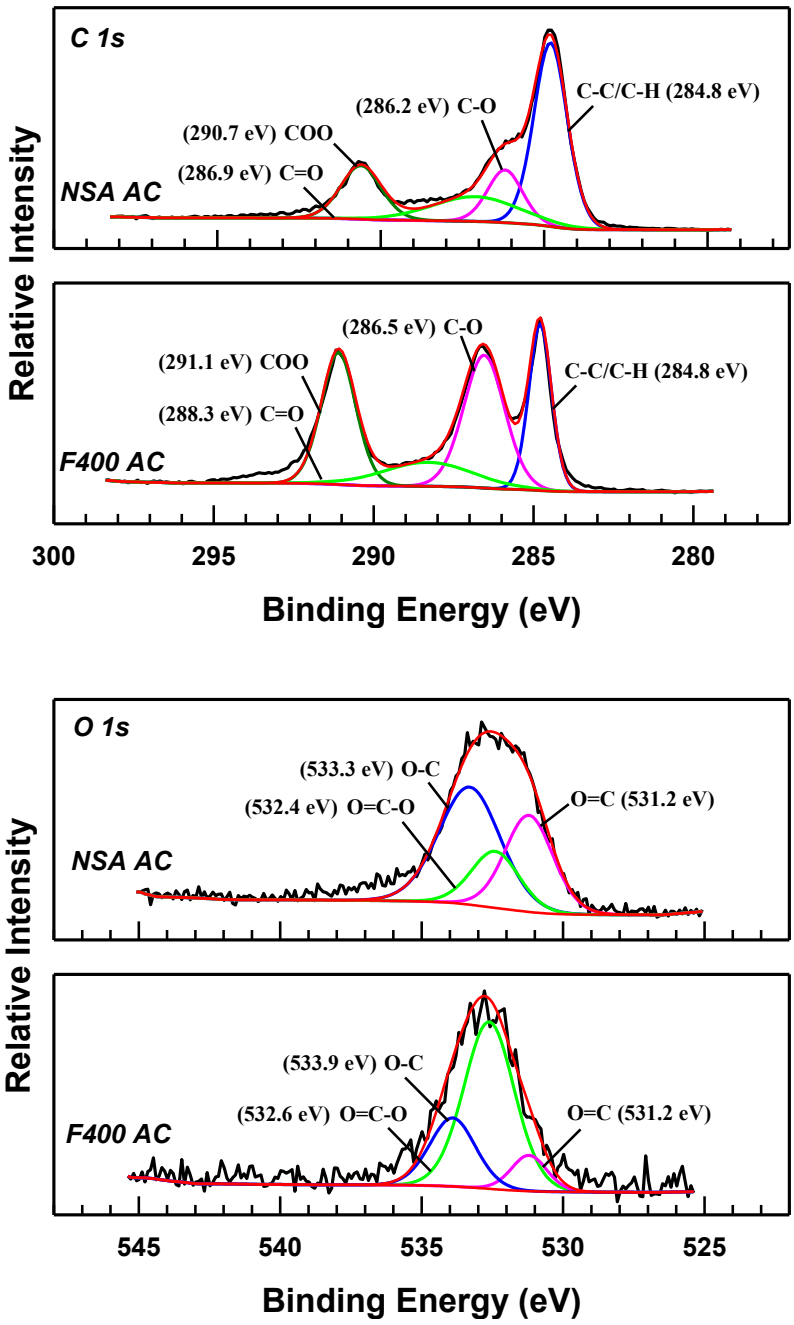

Figure 4.4: XPS spectrum of NSA and F400 activated carbons in terms of C 1s and O 1s chemical states

4.1.4 Zeta Potential

Two kinds of activated carbon were studied: NSA (L-type) and F400 (H-type) [9]. With ionized surface (CO^-), L-type carbons contain negative charges and ample oxygen-containing groups on its surface while the protonated surface ($C\text{-}OH_2^+$) of H-type carbons has a reduced surface with more positive charges [51]. Fig. 4.5 shows the zeta potential of NSA and F400 samples as a function of pH with NaCl concentration (or ionic strength) of 10^{-2}-10^{-1} M. Results show negative zeta potential in a wide range of pH and a pH_{pzc} around pH 3 for NSA. This is similar to that in the literature [45]. On the other hand, the pH_{pzc} around pH 6 for F400 is slightly lower than pH_{pzc} around pH 7 for the Electrophoretic mobility measurements in the literature [9]. The surface of F400 could be gradually oxidized upon exposure to air atmosphere or during the grinding process, which turns out a lower pH_{pzc}.

Usually, pH_{pzc} obtained by electrophoretic mobility measurement (zeta potential) will be lower than pH_{pzc} measured from alkalimetric titration. Due to slowly oxidation of external carbon surface, electrophoretic mobility measurement which detects the potential of shear plane, yields a lower value of pH_{pzc}. Though alkalimetric titration involves the interaction of H^+ and OH^- in both internal and external carbon surface, resulting in higher pH_{pzc} [9]. Thus the pH_{pzc} value for F400 in this study is lower than those reported in the literature [9] [52]. However, the trend that NSA has lower pH_{pzc} than F400 is still true in the zeta potential measurements.

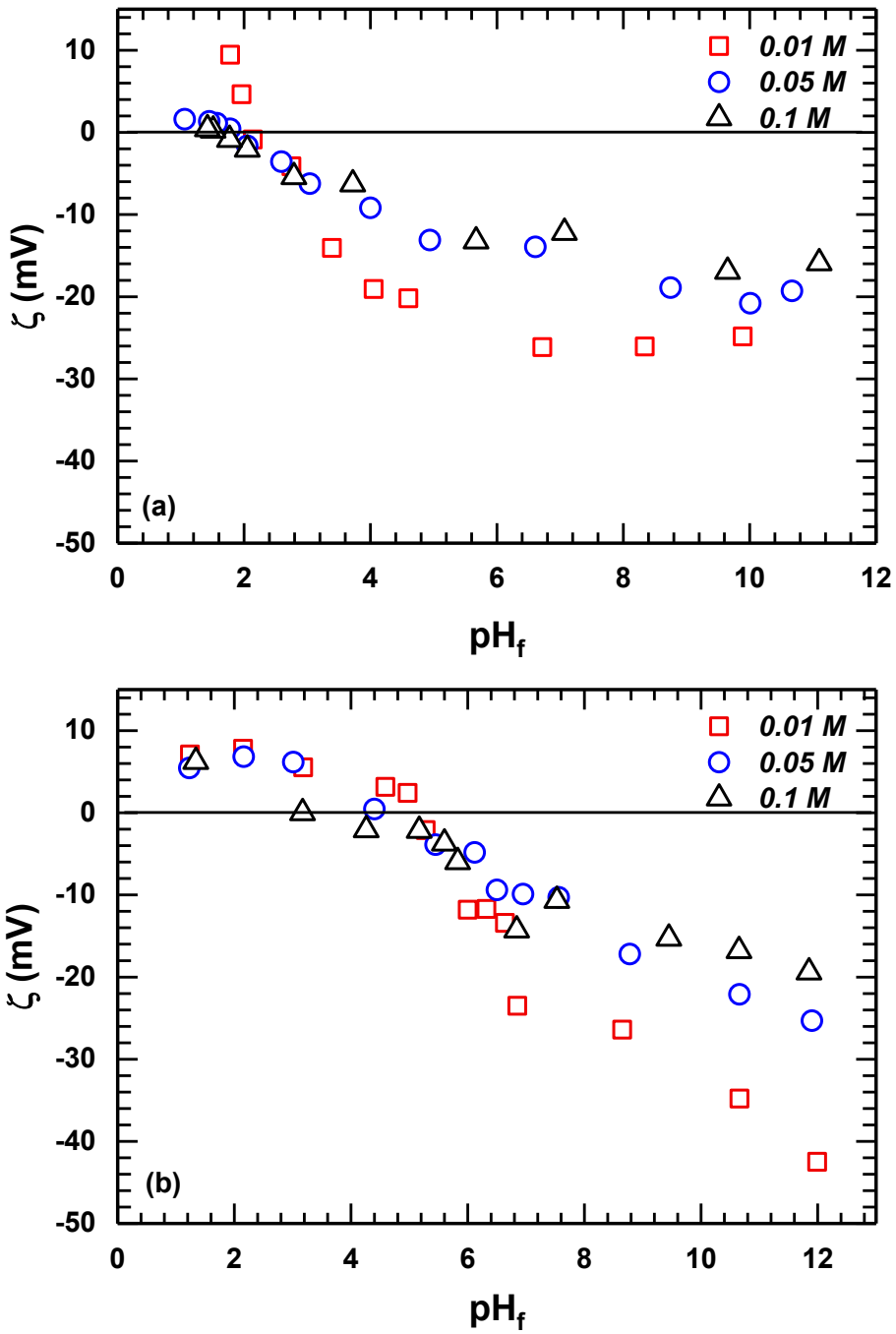

Figure 4.5: Zeta potential of (a) NSA and (b) F400 activated carbons. Experimental conditions: final pH = 1.0 to 12.0, [I] = 0.01-0.1 M NaCl

4.2 Batch Eletro-sorption of Sodium Chloride by NSA/G Electrode

Table 4.2 shows the comparison of experimental methods and electro-sorption performance in CDI with various carbon electrodes. It can be concluded that most CDI studies only recorded cell voltages in the two-electrode system. In addition, cyclic voltammetry is the most common method used to measure the average specific capacitance of the electrodes at a certain scan rate. Also, the majority of research measured conductivity difference and calibrated it into concentration to determine the electro-sorption capacities of the electrodes. However, in this way, we cannot know the exact voltage applied on the electrode, which is a crucial factor in investigating electro-sorption performance. Besides, according to the electrocapillary theory, differential capacitance is a function of potential, being related to the electronic charges of carbon surface, immobile chemical charges in the porous structure, and mobile ionic charges in the solution [53]. Thus instantaneous capacitance calculated by eq. (3-4) should be a better way for analyzing the property of electric double layer on the electrode. Finally, conductivity measurements for electro-sorption capacity are based on the assumption of symmetric adsorption of anions and cations, which lacks for the information of actual removal of anions and cations respectively.

Gabelich et al. showed that solution pH changed after the electro-sorption of NaCl, which may affect the conductivity values of solution. Thus the conductivity measurement they used to decide ion sorption capacities may not be very accurate. In this study, we recorded the initial and final conductivity, pH, and respective concentrations for sodium and chloride ions during electro-sorption processes. A three-electrode system was used to determine the absolute voltage applied on the working electrode and explore the instantaneous capacitance of CDI varying with applied potentials.

Table 4.2: Comparison of experimental methods and electro-sorption performance in CDI with various carbon electrodes

Electrode material	Experimental condition	Initial [NaCl] (mg/L)	Electro-sorption capacitance, C		NaCl removal measurement		Ref.
			Method	Value (F/g)	Method	Value (mg/g)	
ZrO_2 nanofiber/AC	2-electrode; 1.2 V	104	CV (aC[1])	869.86	Cond.[3]	16.35	[44]
AC	2-electrode; 1.5 V	200	EIS	56	Cond.	3.68	[54]
Polyaniline/AC (asymmetric)	2-electrode; 1.4 V; (MCDI[4])	600	CV (aC)	90	Cond.	20	[55]
Anionic polymer modified carbon cloth (asymmetric)	2-electrode; 1.2 V	409	-	-	Cond.	7.6	[56]
Carbon nanosheet	2-electrode; ~1.1 V	500	-	196	Cond.	15.6	[57]
Nano-titanium carburizing electrodes	2-electrode; 1.4 V	50	CV (aC)	56.2	Cond.	9.6	[58]
Graphene	2-electrode; 1.8 V	8	Galvanostatic charge/discharge	189	Cond.	14.25	[59]
Nitrogen-doped carbon spheres	2-electrode; 1.6 V	100	CV (aC)	179	Cond.	11.5	[60]
Carbon xerogel/carbon cloth (asymmetric)	4-electrode; 0 V; (iCDI[5])	251	I/ν (iC[2])	~ ±30 (Si-CX)	Cond.	~1.7	[21]

Table 4.2 continued.

Electrode material	Experimental condition	Initial [NaCl] (mg/L)	Electro-sorption capacitance, C		NaCl removal measurement		Ref.
			Method	Value (F/g)	Method	Value (mg/g)	
Ag (a[6]), HOMCs (c[7]) (asymmetric)	2-electrode; 1.2 V	58.4	CV (aC)	104.2 (HOMCs)	AA for Na^+	20.82	[61]
TiO_2-modified AC cloth	2-electrode; 1.0 V	5.84	-	-	Cond.	4.38	[62]
CNTs-CNFs	2-electrode; 1.2 V	100	-	-	Cond.	3.32	[63]
AC cloth	2-electrode; 1.5 V	1000 (μS/cm)	CV (aC)	41.5	Cond./ IC for cations	~60% Na^+	[64]
SiO_2/carbon fiber Mg-Al_2O_3/carbon fiber (asymmetric)	3-electrode; -1.5 V	~30	-	-	ICP for cations	82 % Na^+	[65]
AC	2-electrode; 1.2 V	292	-	-	Cond./ IC for anions	9.63 Cl^-	[66]
Carbon aerogel	2-electrode; 2.0 V	292	-	-	Cond.	75.97	[67]
Nafion-AC (asymmetric)	2-electrode; 30 mA/g (CC)	500	CV (aC) /EIS	148	Cond.	10.8	[68]
AC-QPVP (a) AC-HNO_3 (c) (asymmetric)	2-electrode; 0 V (iCDI)	500	EIS (iC)	-	Cond.	9.6	[53]

Table 4.2 continued.

Electrode material	Experimental condition	Initial [NaCl] (mg/L)	Electro-sorption capacitance, C		NaCl removal measurement		Ref.
			Method	Value (F/g)	Method	Value (mg/g)	
AC	2-electrode; 1.2 V	100	CV(aC)	101	Cond.	7.71	[69]
Graphene	2-electrode; 2.0 V	25	CV(aC)	140	Cond.	1.35	[11]
AC (asymmetric)	3-electrode; -0.7 V	58.4 (pH 10)	I/ν (iC)	~102 (C_c) ~78 (C_a)	IC for Na^+, Cl	5.44 Na^+	This study

[1]aC = average capacitance. [2]iC = instantaneous capacitance. [3]Cond. = conductivity. [4]MCDI = membrane CDI.

[5]iCDI = inverted CDI. [6]a = anode. [7]c = cathode.

4.2.1 Indirect Measurement-Conductivity

To compare with other studies measuring salt removal in CDI processes by the conductivity difference, initial and final solution conductivities were recorded during the electro-sorption of NaCl and shown in Table 4.3. The relationship between solution conductivity and NaCl concentration is obtained according to the calibration table made prior to the experiment. The amount of NaCl removal was calculated in terms of adsorption capacity by the following equation:

$$\Gamma_e = \frac{(C_0 - C_e) \times V}{m} \quad (4\text{-}1)$$

where Γ_e (mmol/g) is the equilibrium adsorption density, C_0 (mM) is the initial concentration, C_e (mM) is the equilibrium (or final) concentration, V (L) is the volume of solution, and m (g) is the mass of AC on the electrode.

Table 4.3 shows the initial and final solution conductivities with NaCl adsorption density from the electro-sorption of 1 mM NaCl for 80 min by the NSA/G electrode. The NaCl removal derived from conductivity measurements calculated by eq. (4-1) show negative values and very little adsorption density (-0.271~-0.072 mmol/g) comparing to the amounts of adsorbed sodium and chloride ions measured directly by IC. Since much more Na^+ ions (0.158 ~ 0.086 mmol/g) and Cl^- ions (0.008 ~ -0.012 mmol/g) were removed in the same experiments from direct measurements shown in Fig. 4.11 (b), the resulting NaCl removal from conductivity measurements are problematic. In addition, indirect conductivity measurement is based on the assumption of symmetric adsorption of Na^+ and Cl^- ions and ignores the change of solution pH, it cannot differentiate the exact adsorption amounts of Na^+ and Cl^- ions, which may vary depending on electrode materials. Furthermore, the estimated number of NaCl

adsorption density from solution conductivities may also be affected by the pH change shown in Table 4.3, leading to inaccurate evaluation of salt removal.

In the theoretically aspect, the ideal electrolytic conductivity can be calculated by the following equations according to the definition [39]:

$$\mu = z_+ \nu_+ \lambda_+ + z_- \nu_- \lambda_- \quad (4\text{-}2)$$

$$\lambda_T = \Sigma C_i \mu_i = C_i z_+ \nu_+ \lambda_+ + C_i z_- \nu_- \lambda_- \quad (4\text{-}3)$$

Based on the values of limiting ionic conductivity at infinite dilution in aqueous solutions at 298K, λ_0 (S-cm^2/equiv) = 50.11 for Na^+, λ_0 = 76.34 for Cl^-, λ_0 = 349.82 for H^+, and λ_0 = 198 for OH^-, the total conductivity, λ_T (S-cm^{-1}), of 1 mM NaCl solution at pH 6.5 can be calculated theoretically:

$$\lambda_T = \Sigma C_i \mu_i = C_{Na^+}\mu_{Na^+} + C_{Cl^-}\mu_{Cl^-} + C_{H^+}\mu_{H^+} + C_{OH^-}\mu_{OH^-} \quad (4\text{-}4)$$

$$= \left(\frac{10^{-3}}{1000} \times 1 \times 1 \times 50.11\right) + \left(\frac{10^{-3}}{1000} \times 1 \times 1 \times 76.34\right)$$

$$+ \left(\frac{10^{-6.5}}{1000} \times 1 \times 1 \times 349.82\right) + \left(\frac{10^{-7.5}}{1000} \times 1 \times 1 \times 198\right)$$

$$= 126.57 \times 10^{-6} = 1.27 \times 10^{-4} \text{ (S-cm}^{-1}\text{)}$$

In order to investigate how ions contribute to the solution conductivity, the concentrations of ions appearing in the NaCl solution measured by IC and pH meter and also their corresponding conductivities calculated by eq. (4-4) are listed in Table 4.4 for comparison with the measured solution conductivities. As can be seen in Table 4.4, the total conductivities calculated from initial and final ion concentrations and their trends are similar to the solution conductivity measured by the conductivity meter at different applied voltages, suggesting that the theoretically calculated conductivity by eq. (4-4)

are highly correlated to the actual solution conductivities. The Na^+ concentration decreased and H^+ concentration increased after electro-sorption with less variation in chloride and OH^- concentrations, resulting in the increase of final conductivities. Although the amounts of sodium ions reduced were larger than the amounts of proton increased, the calculated final conductivities still increase because of the high limiting ionic conductivity (λ_0) of H^+. Same results also appeared in the measured conductivities.

The results from Table 4.3 demonstrate that conductivity is not only contributed from Na^+ and Cl^- ions, H^+ and OH^- in aqueous solution also have significant influence on it. Therefore, the method used to calculate NaCl removal by calibrating solution conductivity into NaCl concentration without considering pH variation in Table 4.3 is unreliable. Even though the solution conductivity increased after the electro-sorption, Na^+ and Cl^- ions were stilled removed. And the amounts of ion removal were calculated according to the initial and final sodium and chloride concentrations obtained from IC shown in Table 4.4, whose values are much higher than the NaCl removal in Table 4.3 derived from conductivity measurements.

In addition, the removal of Na^+ and Cl^- ions at the same applied voltage but with opposite sign should be equal based on the assumption of symmetric adsorption. However, the removal of Na^+ at $E\text{-}E_{pzc}$ = -0.4 V is a lot higher than the removal of Cl^- at $E\text{-}E_{pzc}$ = 0.4 V shown in Fig. 4.11 (b). Hence, the assumption of symmetric adsorption of anions and cations followed by the indirect conductivity measurement is not applicable in this study. The difference between initial and final conductivities measured in NaCl solution during electro-sorption processes should not be simply converted into equal molar of sodium and chloride ions being adsorbed as lots of literatures have done.

To conclude, individual ion concentrations should be measured directly in order to evaluate actual amounts of Na^+ and Cl^- removal. The conductivity measurement of NaCl removal which cannot differentiate the contribution of different ions is inaccurate. And the assumption of symmetric adsorption on NaCl depends on different electrode materials which should not be applied to every electrode.

Table 4.3: Experimental results from the electro-sorption of 1 mM NaCl for 80 min by the NSA/G electrode using indirect conductivity measurement

$E-E_{pzc}$ (V)	Cond. (i) (μS/cm)	Cond. (f) (μS/cm)	pH_i	pH_f	NaCl removal (mmol/g)
-1.0	128.1	245.0	5.81	3.37	-0.271
-0.8	118.7	207.0	6.36	3.61	-0.205
-0.6	116.8	147.8	6.07	3.98	-0.072

[1] i and f represent initial and final respectively.

Table 4.4: Experimental results from the electro-sorption of 1 mM NaCl for 80 min by the NSA/G electrode using direct IC measurement

$E-E_{pzc}$ (V)		Concentration (mM)				Conductivity (μS/cm)		Ion removal (mmol/g)	
	i/f[1]	Na^+	Cl^-	H^+	OH^-	Calc.[2]	Meas.[3]	Na^+	Cl^-
-1.0	i	0.95	0.96	0.0016	$6.5x10^{-6}$	121.5	128.1	0.16	0.008
	f	0.45	0.94	0.43	$2.3x10^{-8}$	243.2	245.0		
-0.8	i	0.99	0.95	0.0004	$2.3x10^{-5}$	122.5	118.7	0.12	-0.011
	f	0.63	0.99	0.25	$4.1x10^{-8}$	192.3	207.0		
-0.6	i	1.13	0.80	0.0009	$1.2x10^{-5}$	118.0	116.8	0.084	-0.003
	f	0.86	0.81	0.11	$9.6x10^{-8}$	141.7	147.8		

[1] i and f represent initial and final respectively. [2]Calc. = calculation.

[3]Meas. = measurement.

4.2.2 Direct Measurement-Effect of Initial Sodium Chloride Concentration

The results of zeta potential measurements indicated the surface of NSA/G electrode is negatively charged over a wide range of solution pH suggesting that the electrode may be more favorable on the adsorption of positively charged ions. Plus, sodium adsorption is a lot more evident than chloride adsorption by the NSA/G electrode in different experimental conditions which will be discussed in later section. Here we discuss sodium adsorption by the NSA/G electrode first.

Fig. 4.6 shows the effect of initial electrolyte (NaCl) concentration on Na^+ removal by NSA/G electrode as a function of time. Results show that the percentage of sodium decreased in a faster rate at the beginning and became slower during charging of -0.3V (vs. SCE) in 80 min. Besides, more than 90% of Na^+ uptake onto the electrode was released into the solution during desorption when reversing the potential to +0.3V (vs. SCE) for another 80 min. The profile also indicates a lower removal percentage of Na^+ in a higher initial NaCl concentration during the adsorption process.

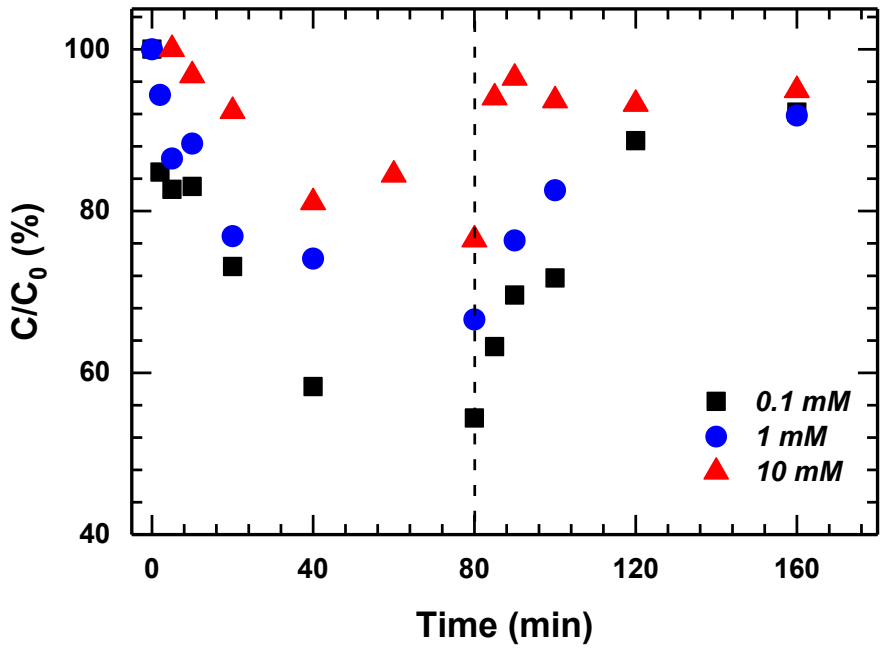

Figure 4.6: Percent remaining for sodium ions as a function of time by the NSA/G electrode. Experiment conditions: initial [NaCl] = 0.1, 1,10 mM, working potential = -0.3 V vs. SCE for adsorption, and +0.3 V vs. SCE for desorption at pH_i= 6.5

4.2.3 Adsorption Isotherms

A series of electro-sorption experiments were run at different initial NaCl concentrations (0.1- 30 mM) in certain adsorption time periods to assess the absolute amount of Na^+ removal and establish Na^+ adsorption isotherms. Fig. 4.7 (a) and Fig. 4.8 (a) show adsorption density of Na^+ as a function of equilibrium sodium concentration fitted by two widely used adsorption models, Langmuir and Fruendlich adsorption isotherms. Results show higher Na^+ uptake in higher sodium concentration in both short and long adsorption periods. In addition, Langmuir adsorption isotherm fitted the Na^+

adsorption better in 80 min while Fruendlich adsorption isotherm fitted the adsorption data in 10 min better as evidenced of larger r^2 value in Table 4.5.

Considering Langmuir isotherm for monolayer adsorption, the amount of adsorbate on the electrode surface can be expressed as the following equation [70]:

$$\Gamma_e = \frac{\Gamma_{max} K_L C_e}{1 + K_L C_e} \tag{4-5}$$

values of K_L and Γ_{max} can be determined graphically by linearizing eq. (4-5):

$$\frac{C_e}{\Gamma_e} = \frac{1}{\Gamma_{max} K_L} + \frac{C_e}{\Gamma_{max}} \tag{4-6}$$

where C_e = equilibrium Na^+ concentration (mmol/L) in the solution, Γ_e = equilibrium Na^+ adsorption density (mmol/g) on the electrode surface, Γ_{max} = maximum Na^+ adsorption density (mmol/g) for saturated monolayer coverage, and K_L = Langmuir constant (L/mmol) and is an affinity parameter related to the bonding energy to the surface [71]. By plotting C_e/Γ_e versus C_e, Γ_{max} is equal to the inverse of the slope and K_L can be determined from the intercept shown in Fig. 4.7 (b).

On the other hand, the empirical Freundlich isotherm considered as a multi-layer process can be employed to predict the increasing adsorbate on a heterogeneous surface as the solution concentration increases by the following equation [72]:

$$\Gamma_e = K_F C_e^{1/n} \tag{4-7}$$

values of K_F and n may be calculated by taking the logarithm of eq. (4-7)

$$\log \Gamma_e = (1/n) \log C_e + \log K_F \tag{4-8}$$

where C_e and Γ_e have the same definitions as in the Langmuir isotherm, n = adsorption intensity and 1/n is a function of the strength of adsorption in the adsorption process;

K_F = Freundlich constant ($L^{1/n}$ $mmol^{(1-1/n)}g^{-1}$) and is an indicator of adsorption capacity [73]. By plotting log Γ_e versus log C_e, n is equal to the inverse of the slope and K_F can be determined from the intercept shown in Fig. 4.8 (b). The situation n>1 is most common indicating a normal adsorption and a favorable sorption process lies between 1<n<10. Furthermore, 1/n is also a heterogeneity parameter where the smaller 1/n, the greater the expected heterogeneity [71].

Table 4.5 summarizes the parameters derived from fitting Na^+ adsorption data with Langmuir and Freundlich models to explain the adsorption performance of Na^+ on the NSA/G electrode. Different models were predominated in different adsorption time periods implying that both models may partly represent the adsorption of Na^+. The large r^2 value of 0.99 in Table 4.5 suggests the applicability of the Langmuir isotherm and the maximum adsorption density (Γ_{max}) observed was 0.982 mmol/g for 80 min adsorption. In the meantime, better fitting of Freundlich model in 10 min adsorption denotes the heterogeneous adsorption of Na^+ from aqueous solution by NSA/G electrode [74]. This may due to the heterogeneity nature of NSA activated carbon [75] and the electrical charging to create the variety of sites with different adsorption energy from the electro-sorption process. [6]

Table 4.5: Summary of parameters from Fig. 4.7 and Fig. 4.8 fitted with the adsorption models

	Monolayer Langmuir			Freundlich		
Time (min)	Γ_{max} (mmol/g)	K_L (L/mol)	r^2	K_F ($L^{1/n}$ $mmol^{(1-1/n)}g^{-1}$)	n	r^2
80	0.98	0.231	0.99	0.107	1.425	0.96
10	0.23	0.138	0.91	0.0254	1.647	0.97

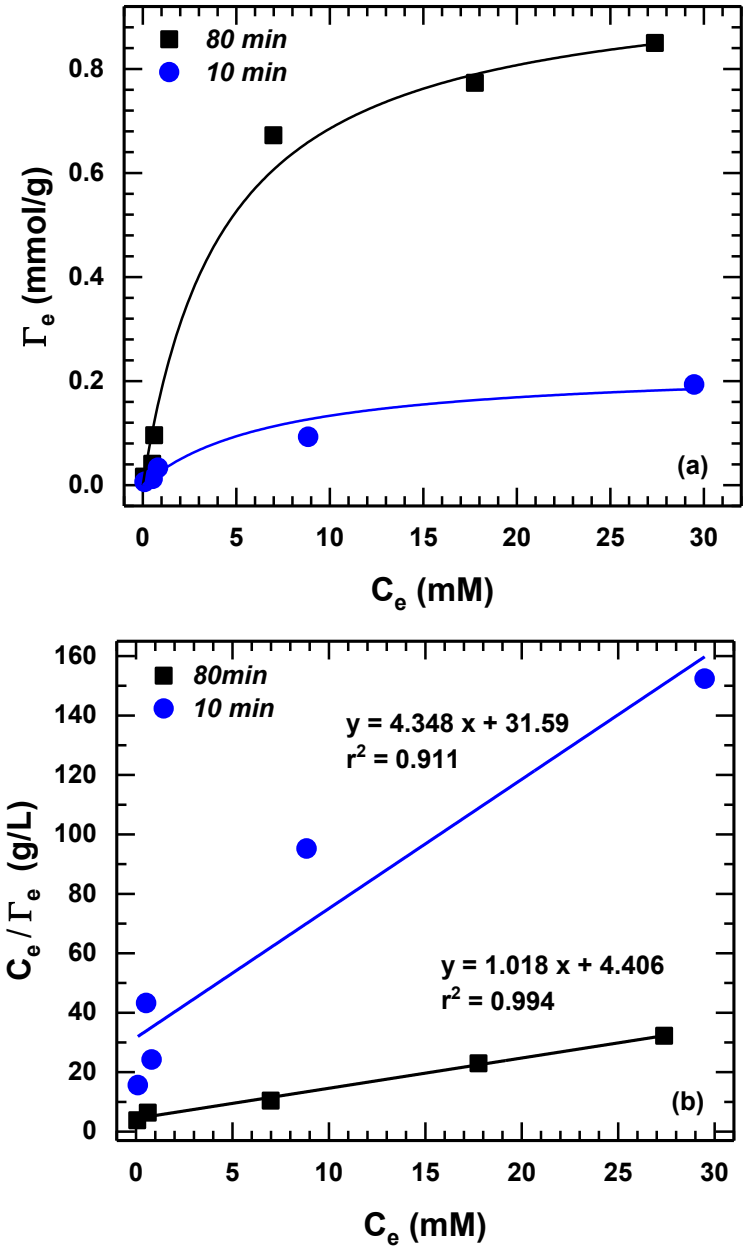

Figure 4.7: (a) Adsorption density of Na^+ as a function of equilibrium sodium concentration and (b) linear fit of the experimental data in (a) by using Langmuir isotherm model. Experimental conditions: initial [NaCl] = 0.1-30 mM, working potential = -0.3 V vs. SCE for 10 min and 80 min respectively by the NSA/G electrode at pH_i= 6.5

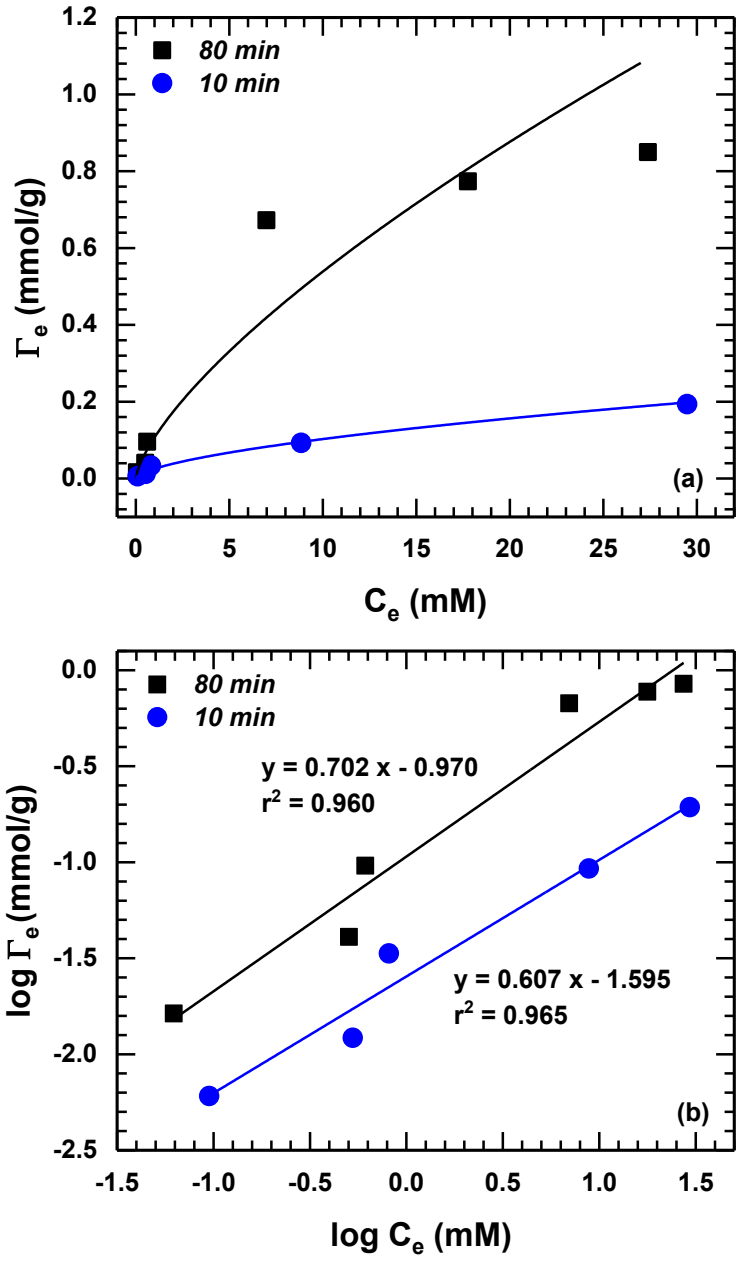

Figure 4.8: (a) Adsorption density of Na^+ as a function of equilibrium sodium concentration and (b) linear fit of the experimental data in (a) by using Frendlich isotherm model. Experimental conditions: initial [NaCl] = 0.1-30 mM, working potential = -0.3 V vs. SCE for 10 min and 80 min respectively by the NSA/G electrode at pH_i= 6.5

4.2.4 Adsorption Kinetics

Since the pseudo-first-order rate equation has been generally applied to describe the adsorption of pollutants from wastewater and the electro-sorption of ions in CDI processes [76][55], the kinetics of Na^+ electro-sorption on the NSA/G electrode was analyzed using pseudo-first-order model presented by Lagergren shown in the following equations [76]:

$$\frac{d\Gamma_t}{dt} = k_1(\Gamma_e - \Gamma_t) \quad (4\text{-}9)$$

where Γ_e and Γ_t (mmol/g) are the adsorption densities at equilibrium and time t (min), respectively, k_1 (min^{-1}) is the pseudo-first-order rate constant. By integrating eq. (4-9) with the boundary conditions including Γ_t=0, at t=0 and $\Gamma_t = \Gamma_t$ at t=t [6], yields

$$\ln\left(\frac{\Gamma_e}{\Gamma_e - \Gamma_t}\right) = k_1 t \quad (4\text{-}10)$$

or can be rearranged to:

$$\log(\Gamma_e - \Gamma_t) = log\,\Gamma_e - \frac{k_1}{2.303}t \quad (4\text{-}11)$$

The adsorption density was calculated by the following equation:

$$\Gamma_t = \frac{(C_0 - C_t)\times V}{m} \quad (4\text{-}12)$$

where C_0 and C_t denote the initial concentration and the concentration (mmol/L) of Na^+ at time t, respectively, V is reaction volume (L), and m is mass of AC on the NSA/G electrode. Finally, the adsorption density profile as a function of time could be written as eq. (4-13) for adsorption kinetics [6]:

$$\Gamma_t = \Gamma_e(1 - e^{-k_{1,ad}t}) \quad (4\text{-}13)$$

For desorption:

$$\Gamma_t = \Gamma_{e,de} + (\Gamma_e - \Gamma_{e,de})e^{-k_{1,de}t} \quad (4\text{-}14)$$

where Γ_e and $\Gamma_{e,\ de}$ (mmol/g) are the adsorption densities of Na^+ at equilibrium of adsorption and equilibrium of desorption, respectively, $k_{1,\ ad}$ and $k_{1,\ de}$ are the adsorption and desorption rate constants, respectively. By plotting "log (Γ_e - Γ_t) versus t" for different concentrations of NaCl, the rate constants determined from the slope along with the corresponding r^2 values are presented in Table 4.6. The adsorption kinetics profiles in different NaCl concentrations fitted with eq. (4-13) and eq. (4-14) are also shown in Fig. 4.9.

The results shown in Fig. 4.9 and Table 4.6 indicate that the adsorption rate decreased when the solution concentration increased. However, Chen et al. [77] reported the opposite result. The discrepancy may be due to the lower values of correlation coefficient (r^2) at 0.1 mM and 10 mM during adsorption, resulting in error when estimating the rate constants. On the contrary, the desorption rate with higher r^2 values increased when the solution concentration increased. This corresponds to that generally increase of solution concentration results in an increase of the driving force, which will increase the diffusion rate of Na^+ [78]. To conclude, the electro-sorption of Na^+ onto NSA/G electrode at 1 mM with the highest r^2 values in both adsorption and desorption processes may follow the pseudo-first-order rate model. The 1mM concentration of NaCl was then chosen to be the experiment condition for later studies.

Table 4.6: Summary of parameters from Fig. 4.9 fitted with pseudo-first-order model

	Adsorption		Desorption	
NaCl (mM)	$k_{1,ad}$ (min^{-1})	r^2	$k_{1,de}$ (min^{-1})	r^2
0.1	0.0574	0.891	0.044	0.964
1	0.0548	0.933	0.050	0.999
10	0.0281	0.909	0.605	0.982

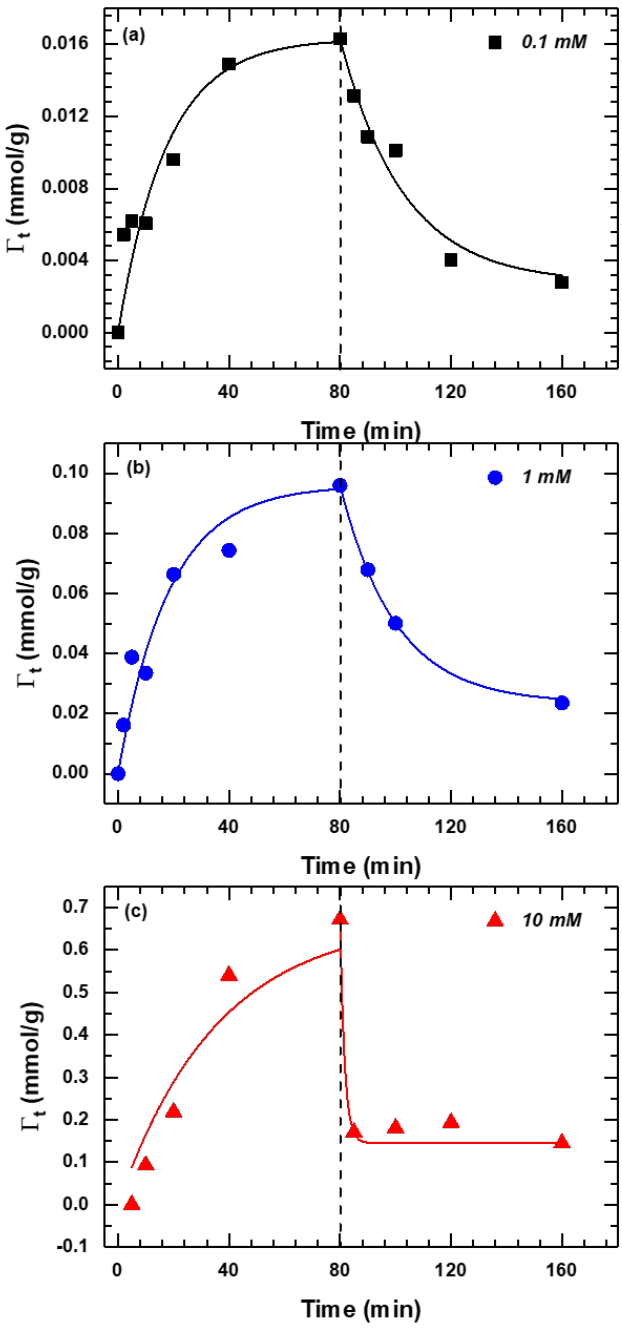

Figure 4.9: Adsorption density of Na^+ as a function of time by the NSA/G electrode. Data fitted by pseudo-first-order rate model. Experiment conditions: initial [NaCl] = 0.1, 1, 10 mM, working potential = -0.3 V vs. SCE for adsorption, and +0.3 V vs. SCE for desorption at pH_i = 6.5

4.2.5 Direct Measurement-Effect of Applied Potential and Solution pH

Fig. 4.10 shows the adsorption density for sodium and chloride ions as a function of applied potential by NSA/Graphite electrode in different solution pH. The applied potential was referenced both to a SCE and the potential of zero charge, E_{pzc} = 0.3 V. It is seen that sodium adsorption is a lot more evident than chloride adsorption especially in negative potentials for all three pH conditions which are also shown in Fig. 4.11. The lines in Fig. 4.11 are for the guidance of data points above the E_{pzc}. The chloride adsorption did not increase even in more positive potentials which may due to the negatively-charged surface of the NSA/G electrode. Therefore, we will focus on discussing only the adsorption of sodium ions in the following sections.

Fig. 4.12 (a) shows the effect of initial pH on the electro-sorption of sodium ions by NSA/G electrode as a function of applied potential. Results show that applied potential and pH play important roles in Na^+ adsorption. As all data points were derived in 1mM NaCl solution for 80-min adsorption, it is not surprising that adsorption of Na^+ increased with increasing applied potential to more negative for all three pH values. And sodium adsorption density shows nearly zero or negative under positive potentials. The other significant parameter that affects the adsorption of Na^+ is the initial solution pH. The pH_{pzc} of NSA activated carbon measured from zeta potential is around pH 3. And it shows that sodium removal decreases when the initial pH was lower and close to the pH_{pzc} of NSA at a certain applied potential.

To consider the two main factors that influence the adsorption of sodium ions, the total adsorption density of sodium, Γ_e is separated into two parts and expressed as the sum of sodium adsorption density derived from the potential effect (polarizable interface), Γ_E, and sodium adsorption density derived from the pH effect (reversible interface), Γ_{pH}, which can be written,

$$\Gamma_e = \Gamma_E + \Gamma_{pH} \quad (4\text{-}15)$$

Then the values of total sodium adsorption density (mmol/g) were transferred into total sodium charge density (C/g), σ_{Na^+}, on the electrode surface shown in Fig. 4.12 (b) to be furthered analyzed for the contribution of pH effect and potential effect on the total amount of sodium adsorption.

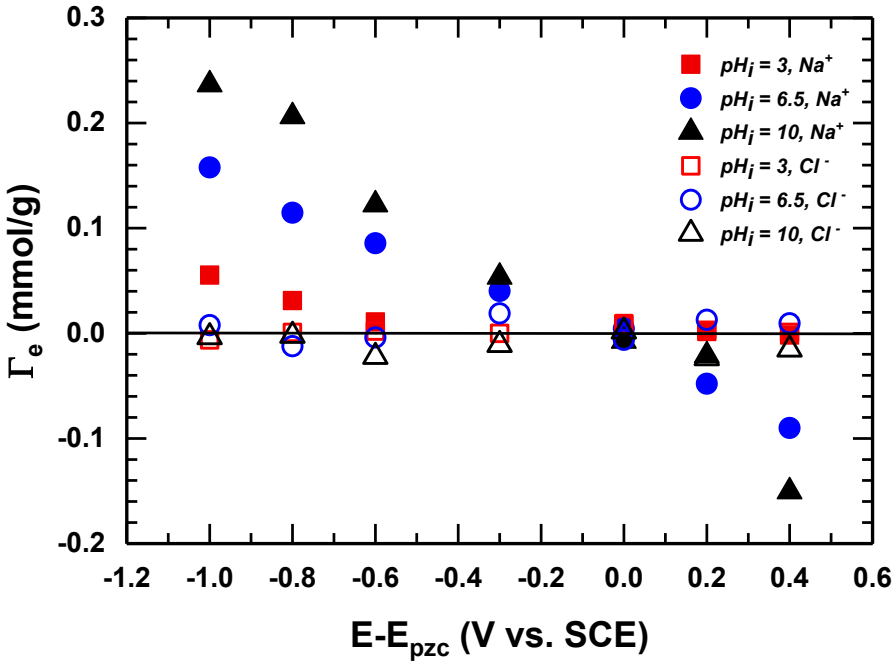

Figure 4.10: Adsorption density of sodium and chloride ions by the NSA/G electrode as a function of E-E_{pzc}. Experiment conditions: initial [NaCl] = 1 mM at different pH values for 80 min adsorption. E_{pzc} = 0.3V (vs. SCE).

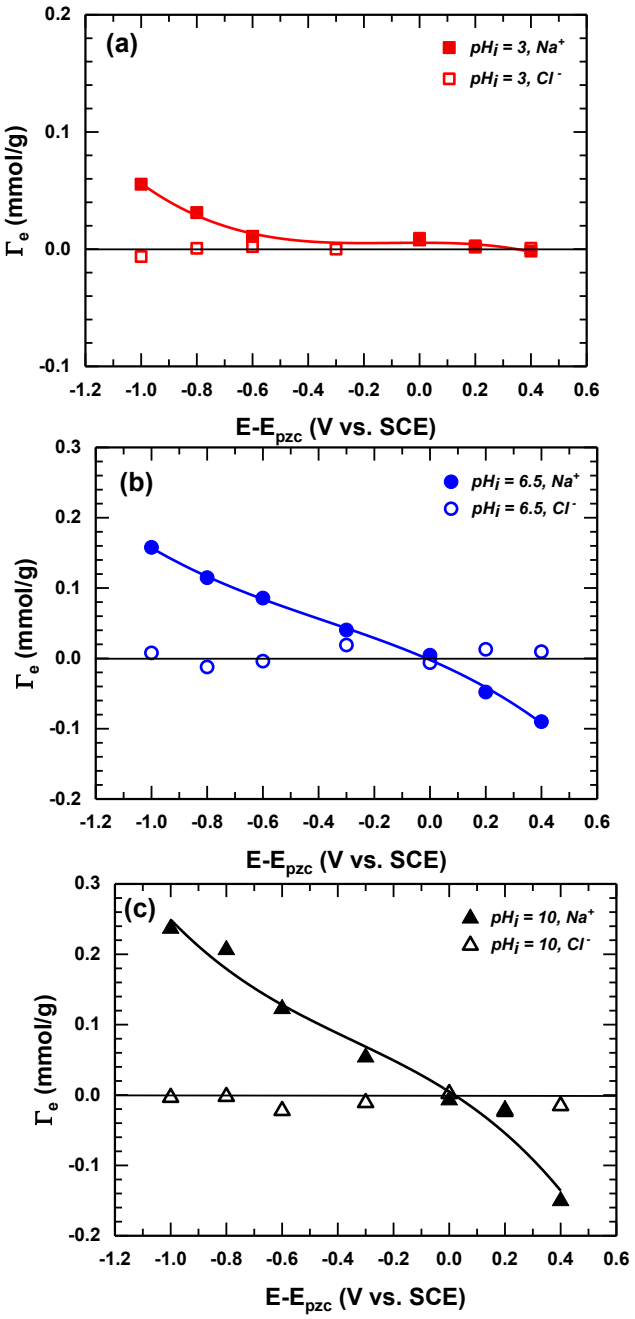

Figure 4.11: Adsorption density of sodium and chloride ions by the NSA/G electrode at initial pH = (a) 3, (b) 6.5, and (c) 10 as a function of E-E_{pzc}. Experiment conditions: initial [NaCl] = 1 mM for 80 min adsorption. E_{pzc}=0.3V (vs. SCE). The lines are only guide to the eye.

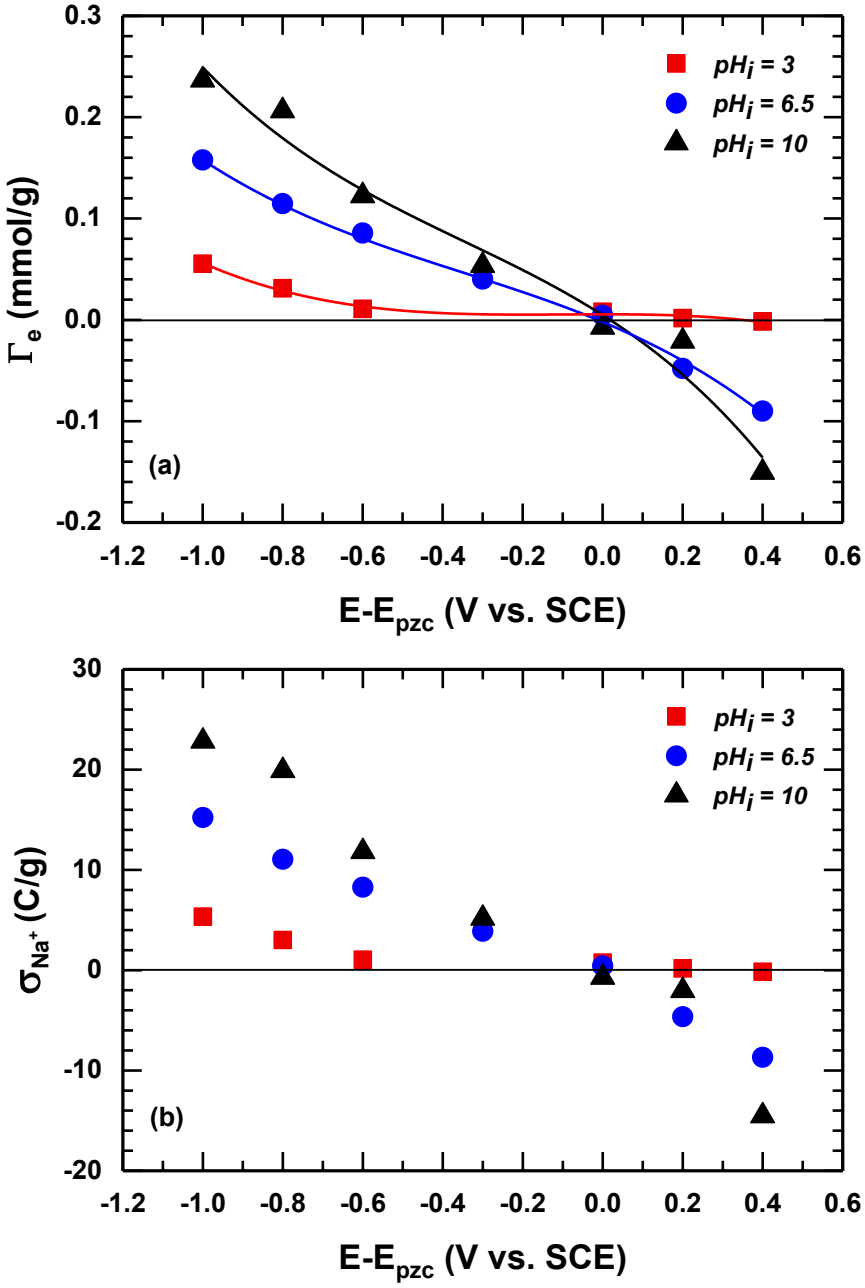

Figure 4.12: Adsorption density of sodium ions by the NSA/G electrode in the units of (a) mmol/g and (b) C/g as a function of E-E_{pzc}. Experiment conditions: initial [NaCl] = 1 mM at different pH values for 80 min adsorption. E_{pzc} = 0.3V (vs. SCE). The lines in (a) are only guide to the eye.

Theoretical estimation of sodium charge density

According to the Gouy-Chapman theory stated in section 2.2 and section 2.4, the relation between surface potential and charge density can be used to predict the sodium charge density on the electrode from the following equations [39]:

$$\sigma^M = -\sigma^S = (8k_bT\varepsilon\varepsilon_0 I)^{1/2}\sinh(\frac{ze\Psi_0}{2k_bT}) \quad (4\text{-}16)$$

For dilute aqueous solutions (ε=78.49) at 25°C, the constants can be evaluated to give

$$\sigma^M = -\sigma^S = 0.117\sqrt{I}\sinh(19.5z\Psi_0) \quad (4\text{-}17)$$

By substituting for Ψ_0 by the applied potential referenced to the potential of zero charge, E_{pzc} (=0.3V vs. SCE), sodium charge density in the solution phase (σ^S, C/m^2) can be predicted. The charge density on the electrode side contributed from potential effect can then be written as a function of applied potential:

$$\sigma_E = 0.117\sqrt{I}\sinh(19.5z\Psi_0^E) \quad (4\text{-}18)$$

where σ_E (C/m^2) is the surface charge and Ψ_0^E (V) is the potential at electrode surface both resulting from the external applied potential.

On the other hand, zeta potential of the NSA/G surface measured in the previous section was considered here to estimate the surface potential on the electrode side for the sake of predicting the sodium charge density derived from pH effect. According to the Gouy-Chapman theory, surface potential at different solution pH can be obtained by the following equations [39]:

$$\tanh\frac{ze\Psi_x}{4k_bT}/\tanh\frac{ze\Psi_0}{4k_bT} = e^{-\kappa x}\ ,\ \kappa = \left(\frac{2Iz^2e^2}{\varepsilon\varepsilon_o k_bT}\right)^{1/2} \quad (4\text{-}19)$$

or

$$\ln\tanh\left(\frac{ze\Psi_x}{4k_bT}\right) = \ln\tanh\left(\frac{ze\Psi_o}{4k_bT}\right) - \kappa x$$

$$\ln\tanh(9.72\Psi_x) = \ln\tanh(9.72\Psi_0) - \kappa x \text{ at } 25°C \quad (4\text{-}20)$$

when the potential at distance x, Ψ_x, is substituted by the zeta potential, ξ, and assume $x = \kappa^{-1}$, eq. (4-20) can be reformulated into

$$\ln\tanh(9.72\xi) = \ln\tanh(9.72\Psi_0) - 1 \quad (4\text{-}21)$$

$$\tanh(9.72\Psi_0) = e^{1+\ln\tanh(9.72\xi)} \quad (4\text{-}22)$$

$$\Psi_0 = \frac{1}{9.72}\tanh^{-1}(e^{1+\ln\tanh(9.72\xi)}) \quad (4\text{-}23)$$

By applying eq. (4-23), surface potential of the electrode can be determined and was shown in Fig. 4.13 (a). Because there is no surface potential data for ionic strength of 10^{-3} M, extrapolation was used in order to evaluate the surface potential in 10^{-3} M under different pH values. Surface potential as a function of the square root of the ionic strength (10^{-1}, 5×10^{-2}, 10^{-2} M NaCl) was shown in Fig. 4.13 (b) for extrapolation. Lastly, the charge density on the electrode side contributed from pH effect can be determined from the surface potential by using eq. (4-24) [39]:

$$\sigma_{pH} = 0.117\sqrt{I}\sinh\left(19.5z\Psi_0^{pH}\right) \quad (4\text{-}24)$$

where σ_{pH} (C/m^2) is the surface charge and Ψ_0^{pH} (V) is the surface potential both resulting from the potential determining species (H^+ and OH^-) in the solution.

Based on eq. (4-15), total sodium adsorption density is the sum of sodium adsorption density derived from potential effect and pH effect. Hence, total charge

density, σ_T (C/m^2), on the electrode surface can also be expressed as the sum of surface charge contributed from potential effect and pH effect by combining eq. (4-18) and eq. (4-24):

$$\sigma_T = \sigma_E + \sigma_{pH} = 0.117\sqrt{I}\sinh(19.5z\Psi_0^E) + 0.117\sqrt{I}\sinh\left(19.5z\Psi_0^{pH}\right) \quad (4\text{-}25)$$

$$\sigma_{Na^+} = -(\sigma_E + \sigma_{pH})$$

$$= -0.117\sqrt{I}\sinh(19.5z\Psi_0^E) - 0.117\sqrt{I}\sinh\left(19.5z\Psi_0^{pH}\right) \quad (4\text{-}26)$$

As long as adding a negative sign to the total charge density on the electrode side, total sodium charge density (C/g) on the solution side, σ_{Na^+}, can be estimated. The calculated σ_{pH}, σ_E, and σ_T at different pH and potentials are shown in Table 4.7.

Fig. 4.14 shows the comparison of calculated charge density obtained from pH effect and potential effect at E-E_{pzc}=-0.3 V. It can be seen that the major amount of surface charge is contributed from the external applied potential for all three pH values. However, the percentage of surface charge and also the actual amount of charge in C/m^2 unit on the electrode derived from pH effect increased as increasing solution pH. This is reasonable since the surface of the NSA/G electrode becomes more negative when being away from the pH_{zpc} in a higher solution pH. The result corresponds with Fig. 4.12 (b) revealing larger adsorbed sodium charge density (opposite signed to the total charge density on the surface) in higher pH values at the same potential.

Fig. 4.15 compares the adsorbed sodium charge density by the NSA/G electrode between the calculation numbers by eq. (4-26) and the values from direct adsorption at the same experimental conditions. It shows that the calculated sodium charge density is much higher than the experimental data in the potential range from -1.0 to 0 V in every

pH. The difference between the maximum sodium charge predicted from theoretical calculation and the realistic values may due to the surface area (1732.63 m^2/g) of NSA AC on the electrode not fully utilized for electro-sorption. The EDL built on the electrode-solution interface is considered as a capacitor and was charging when applying a potential. It may not be absolutely charged through the whole surface area within 80 min thus only adsorbed few sodium ions. Besides, the total sodium charge density predicted from eq. (4-26) has the highest value under pH 3 which is reversed to that from direct electro-sorption. This is caused by the higher ionic strength of pH 3 resulting in more surface charge calculated from the applied potential.

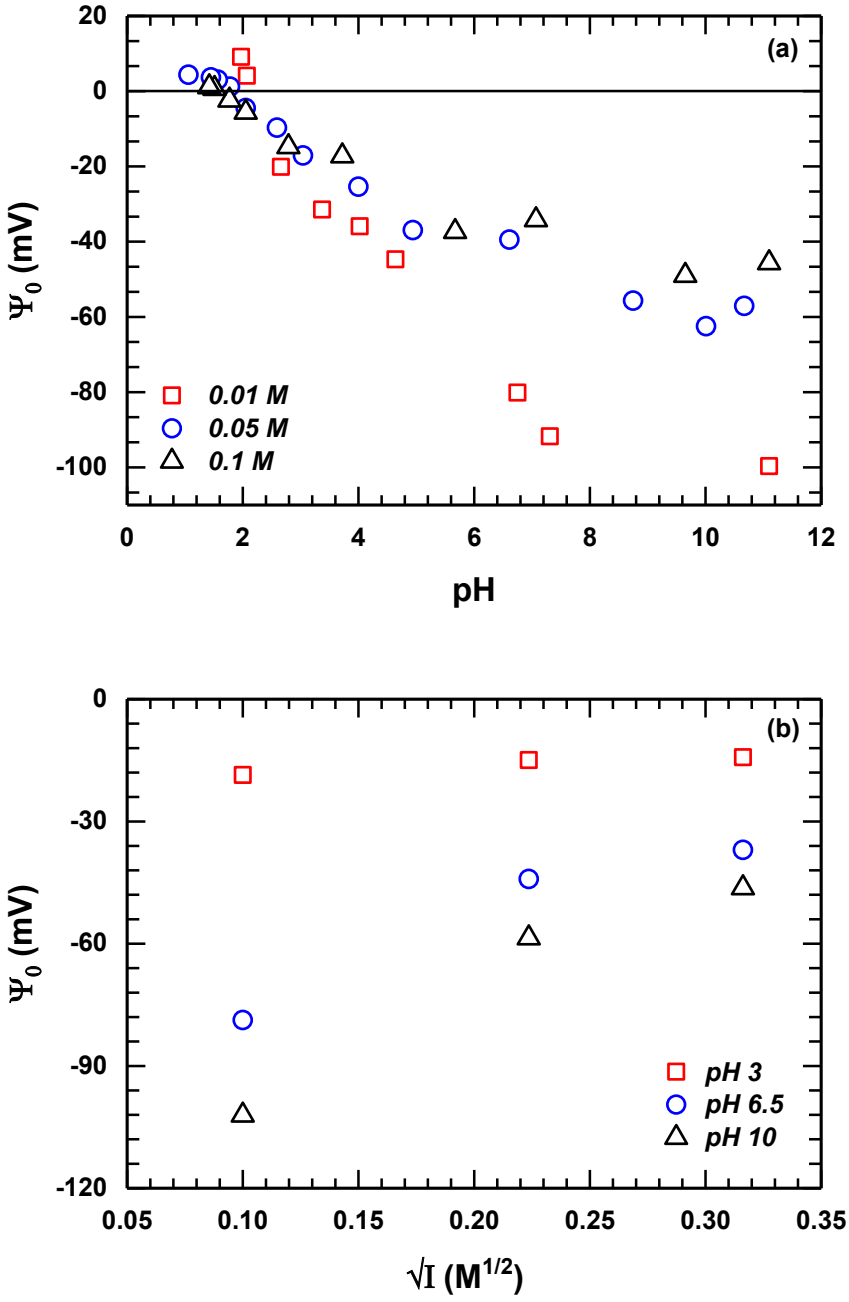

Figure 4.13: (a) Surface potential as a function of pH at [I] = 10^{-1}, 5×10^{-2}, 10^{-2} M NaCl and (b) surface potential as a function of ionic strength at pH 6.5 and pH 10 of the NSA AC.

Table 4.7: Calculated charge density contributed from pH effect and potential effect respectively and the total charge density in 1 mM NaCl on the NSA/G electrode by using eq. (4-25).

$E\text{-}E_{pzc}$ (V) $\equiv \Psi_0^E$		-1.0	-0.8	-0.6	-0.3	0
pH 3	σ_{pH} (C/m^2)	-1.53x10^{-3}	-1.53x10^{-3}	-1.53x10^{-3}	-1.53x10^{-3}	-1.53x10^{-3}
	$\frac{\sigma_{pH}}{\sigma_T}$(%)	1.98x10^{-7}	9.79x10^{-6}	4.83x10^{-4}	0.17	100.00
	σ_E (C/m^2)	-7.70x10^5	-1.56x10^4	-3.15x10^2	-9.08x10^{-1}	0.00
	$\frac{\sigma_E}{\sigma_T}$(%)	100.00	100.00	100.00	99.83	0.00
	σ_T (C/m^2)	-7.70x10^5	-1.56x10^4	-3.15 x10^2	-9.10x10^{-1}	-1.53 x10^{-3}
pH6.5	σ_{pH} (C/m^2)	-1.22 x10^{-2}	-1.22 x10^{-2}	-1.22 x10^{-2}	-1.22 x10^{-2}	-1.22 x10^{-2}
	$\frac{\sigma_{pH}}{\sigma_T}$(%)	2.24x10^{-6}	1.11x10^{-4}	5.46 x10^{-3}	1.86	100.00
	σ_E (C/m^2)	-5.44 x10^5	-1.10 x10^4	-2.23 x10^2	-6.42x10^{-1}	0.00
	$\frac{\sigma_E}{\sigma_T}$(%)	100.00	100.00	100.00	98.14	0.00
	σ_T (C/m^2)	-5.44 x10^5	-1.10 x10^4	-2.23 x10^2	-6.55x10^{-1}	-1.22 x10^{-2}
pH 10	σ_{pH} (C/m^2)	-2.15 x10^{-2}	-2.15 x10^{-2}	-2.15 x10^{-2}	-2.15 x10^{-2}	-2.15 x10^{-2}
	$\frac{\sigma_{pH}}{\sigma_T}$(%)	3.76x10^{-6}	1.86x10^4	9.17 x10^{-3}	3.09	100.00
	σ_E (C/m^2)	-5.71 x10^5	-1.16 x10^4	-2.34 x10^2	-6.74x10^{-1}	0.00
	$\frac{\sigma_E}{\sigma_T}$(%)	100.00	100.00	100.00	96.91	0.00
	σ_T (C/m^2)	-5.71 x10^5	-1.16 x10^4	-2.34 x10^2	-6.95x10^{-1}	-2.15 x10^{-2}

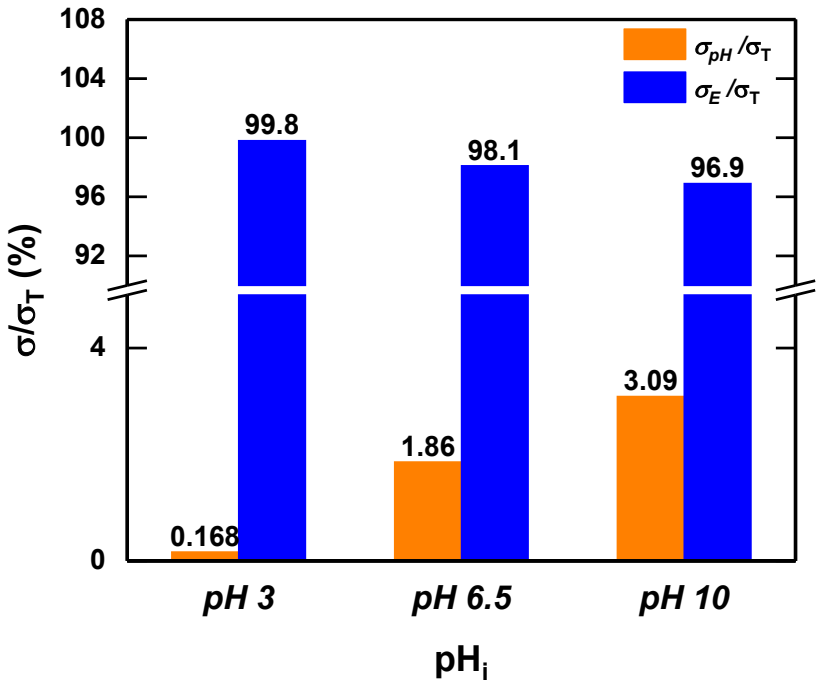

Figure 4.14: Percentage of calculated charge density in 1mM NaCl contributed from pH effect and potential effect respectively in total charge density by the NSA/G electrode at $E-E_{pzc} = -0.3$ V; σ/σ_T is either σ_{pH}/σ_T or σ_E/σ_T.

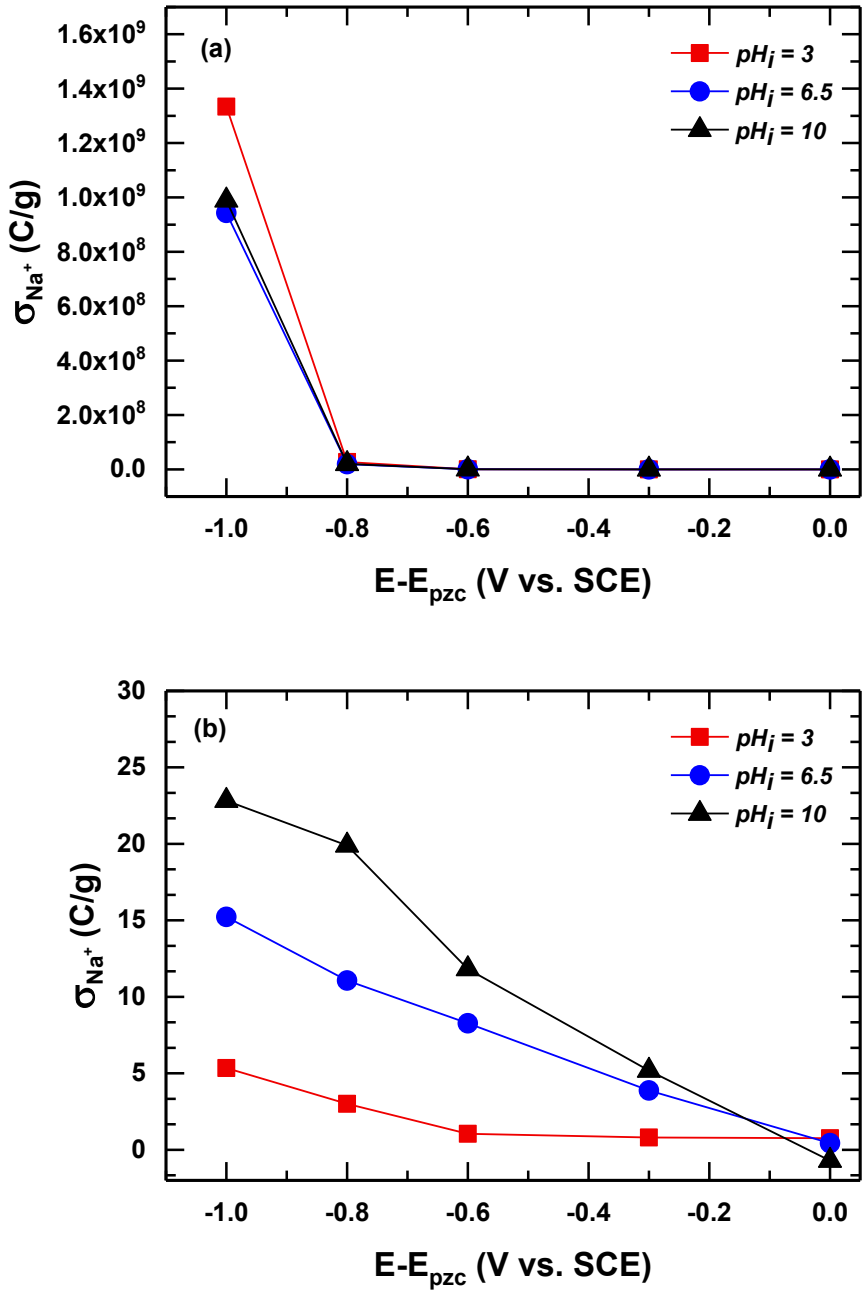

Figure 4.15: Total sodium charge density obtained from (a) calculation by eq. (4-26) and (b) direct adsorption. Experiment conditions: initial [NaCl] = 1 mM for 80 min adsorption by the NSA/G electrode; E_{pzc} = 0.3V (vs. SCE); effective mass of AC= 0.8 g; surface area= 1732.63 m^2/g

pH variation during electro-sorption process

Fig. 4.16 (a) shows the pH variation between initial and final solution pH in different applied potentials. Results show that only at $E-E_{pzc}$ =0, solution pH barely changed after the electro-sorption process. Solution pH decreased and finally stopped at about pH 3 when applying more negative potentials while it increased and approached around pH 10 as applying more positive potential after the electro-sorption in NaCl solution. Reasons that possibly caused the change in solution pH may come from faradaic and/or non-faradaic reactions.

Some common faradaic reactions that may occur on the surface of NSA/G electrode during electro-sorption are summarized in Table 4.8. The standard redox potentials at different pH conditions in Table 4.8 are calculated by the following Nernst equation:

$$E_H = E_H^\circ - \frac{2.303RT}{n_e F} log Q_r \quad (4\text{-}27)$$

which can be written in terms of solution pH:

$$E_H = E_H^\circ - \frac{0.059V}{n_e}\left[log\left(\frac{[Red]^{n_r}}{[Ox]^{n_o}}\right) + n_H pH\right] \quad (4\text{-}28)$$

where E_H° (V) is the standard reduction (or redox) potential measured against the NHE at pH 0, Q_r is the reaction quotient, n_e is the number of electrons transferred, F is the Faraday constant (96485 C mol^{-1}), R is the gas constant (8.314 J K^{-1} mol^{-1}), T (K) is the temperature.

Among the redox reactions listed in Table 4.8, reactions that will produce protons are water oxidation (4-a) and hydrogen oxidation (4-c). However, the NaCl solution in pH range from 3 to 10 contains no hydrogen gas for hydrogen oxidation. The

only possible reaction left is water oxidation which requires 1.052 V ~ 0.639V (vs. NHE) in solution of pH 3 ~ pH 10 according to Table 4.8. The negative applied potentials (-0.3 V ~ -1.0 V vs. SCE or -0.056V ~ -0.76 V vs. NHE) were not high enough to drive the water oxidation reaction though it may happen on the anode (as counter electrode) of an unknown potential in the three electrode system. On the other hand, reactions that will produce hydroxide ions are oxygen reduction (4-b) and water reduction (4-d). But the positive applied potentials (0.2V ~ 0.4V vs. SCE or 0.44V ~ 0.64V vs. NHE) are too high to stimulate both oxygen and water reduction potentials in all three pH conditions. Although for the same reason, those reactions may happen in the cathode (as counter electrode) containing an unknown potential. In order to determine what reactions affected solution pH in the electro-sorption process, further electrochemical investigation of NSA/G electrode will be done in the next section.

Other than faradaic reactions, asymmetry of anion and cation removal and different adsorption rates of H^+ and OH^- ions may also cause the pH fluctuation during the electro-sorption process. Based on higher removal of sodium ion on the cathode than chloride ion on the anode during electro-sorption shown previously in Fig.4.11, a charge imbalance in the solution would be created, resulting in the compensation for positive charges. The system thus tended to produce more protons to offset the charge inequality through water electrolysis [79]. In addition, selective adsorption of H^+ and OH^- may be another reason causing pH evolution because of higher mobility of H^+ than OH^- to the electrode surface [79].These capacitive phenomena without electron-transfer resulting in the imbalance of electro-neutrality can be compensated by faradaic reactions even below the needed redox potentials because CDI is not operating in steady-state [15]. Fig. 4.16 (b) shows an approximate linear relationship and positive correlation between pH

variation and sodium charge density. It again demonstrates that higher sodium adsorption contributes to larger pH difference in all applied potentials which agrees with the inference relating to the non-faradic H^+ production for charge balance

Table 4.8: Standard redox potentials in aqueous solutions at 25°C in V vs. NHE

		E°_H (pH0) (V)	E°_H (pH3) (V)	E°_H (pH6.5) (V)	E°_H (pH10) (V)
$O_2 + 4H^+ + 4e^- = 2H_2O$	(4-a)	1.23	1.05	0.85	0.64
$O_2 + 2H_2O + 4e^- = 4OH^-$	(4-b)	0.40	0.22	0.018	-0.19
$2H^+ + 2e^- = H_2$	(4-c)	0	-0.177	-0.384	-0.590
$2H_2O + 2e^- = H_{2(g)} + 2OH^-$	(4-d)	-0.83	-1.01	-1.21	-1.42
$Na^+ + e^- = Na$	(4-e)	-2.71	-2.71	-2.71	-2.71
$Cl_2 + 2e^- = 2Cl^-$	(4-f)	1.36	1.36	1.36	1.36

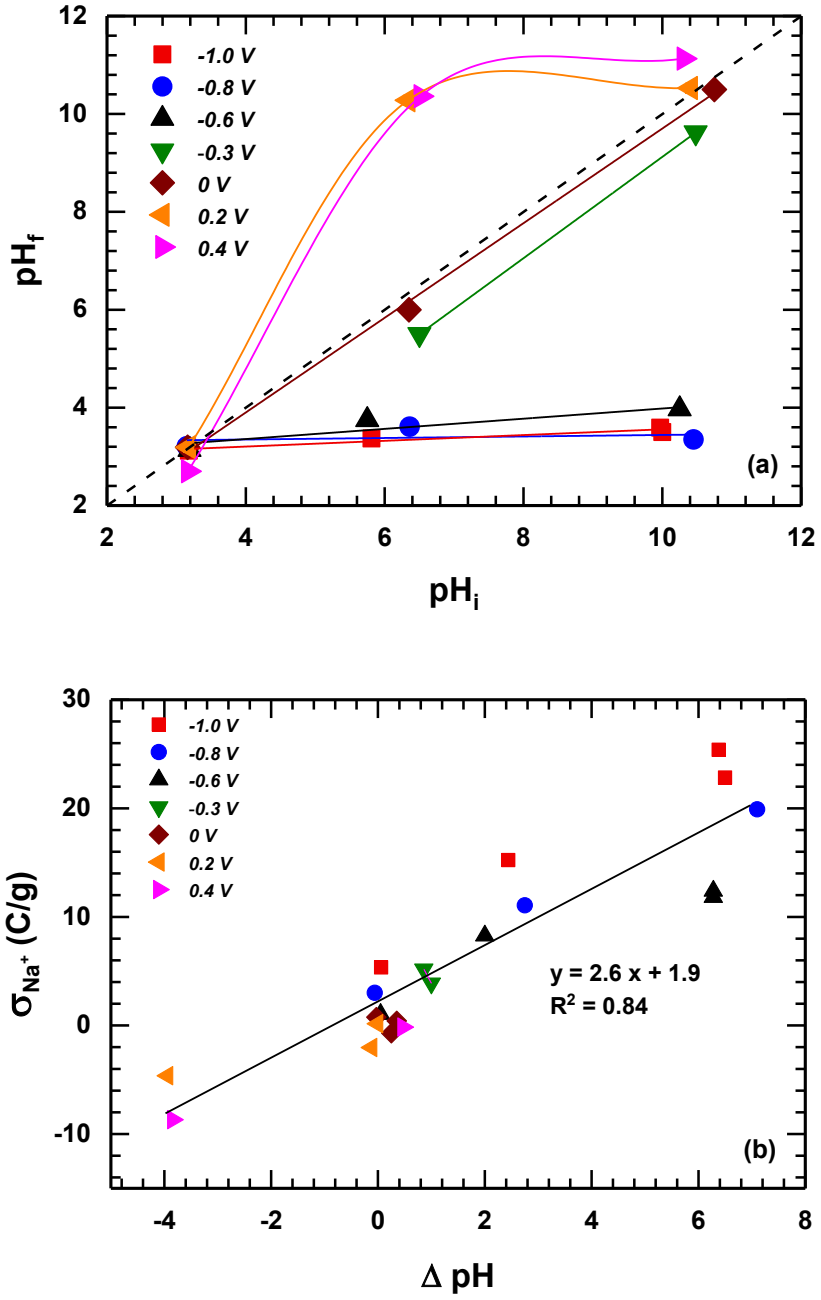

Figure 4.16: (a) pH variation between pH_i and pH_f as a function of $E-E_{pzc}$ (b) total sodium charge density on NSA/G as a function of ΔpH. $\Delta pH = pH_i - pH_f$. Experiment conditions: initial [NaCl] = 1 mM for 80 min adsorption

4.3 Electrochemical Analysis of the NSA /G Electrode

4.3.1 Cyclic Voltammetry

Fig. 4.17 (a) and (b) depict cyclic voltammetry curves for the NSA/G electrode at different scan rates in both low (1 mM) and high (100 mM) electrolyte concentrations within the scan range of -0.9 V and 0.9 V (vs. SCE). The scan range was chosen to include the potential range applied in the electro-sorption experiment in previous section. A remarkable difference between low and high concentrations is that the CV curve in high concentration indicates a quasi-rectangular shape while it is barely seen a rectangular shape in the low concentration. The CV curves tested at scan rates from 2 to 30 mV/s in the high concentration all show capacitive current in the middle region with some Faradaic reactions only observed on both end of the curves.

According to the faradaic reactions listed in Table 4.8, the oxidation peak shown around +0.6 V (or +0.84 V vs. NHE) in 100 mM NaCl solution in Fig. 4.17 (b) should be water oxidation (E_H° = 0.846 V vs. NHE at pH 6.5). And the reduction peak shown around -0.1 V (or +0.14 V vs. NHE) should be water reduction reaction (E_H° = -1.212 V vs. NHE at pH 6.5). Though +0.14 V is higher than the standard water reduction potential, the reaction may still occur due to different nature of Pt electrode in the standard condition and the NSA/G electrode used in this study. Besides, the much higher concentration of H_2O than the other species in the solution will also trigger the water reduction reaction.

On the other hand, in the low concentration of 1mM NaCl solution, only one peak appearing in negative scan direction at around -0.3 V can be observed at a very low scan rate in Fig. 4.17 (a). Electrolyte starvation (or depletion) may explain why no rectangular shape shown in the CV curve. Due to the solution of low concentration

containing insufficient amount of ions that can be adsorbed onto the electrode surface, a current decay from -8 mA to -5 mA arises before the maximum applied voltage is reached in the negative scan of CV [80]. This explanation can be verified by comparing the experimental stored charge from CV to the total available charge (Na^+) in the electrolyte. The charge which was stored over the negative scan (+0.9V to -0.9V vs. SCE) of CV run, was found to be 6.55 (C g^{-1}) from the integration of experimental current-time profile. Meanwhile, the total available charge from the solution of 1mM NaCl is calculated to be 30.15 (C g^{-1}) according to the amount of solution and the electrode mass.

The total available charge calculated from 1mM NaCl solution is more than the charge stored over the negative scan of CV, thus electrolyte depletion cannot explain the peak showing in Fig. 4.17 (a). However, lower diffusion rate of Na^+ ions from the bulk solution caused by the grow of diffusion layer may be the reason. The diffusion layer containing Na^+ ions that are electro-adsorbed to the electrode surface continues to grow upon scanning to more negative potentials. This slows down the diffusion rate of Na^+ ions from the bulk solution to the electrode, resulting in a decrease in the current. The phenomenon is more evident in slower scan rate with longer time for the diffusion layer to grow [81].

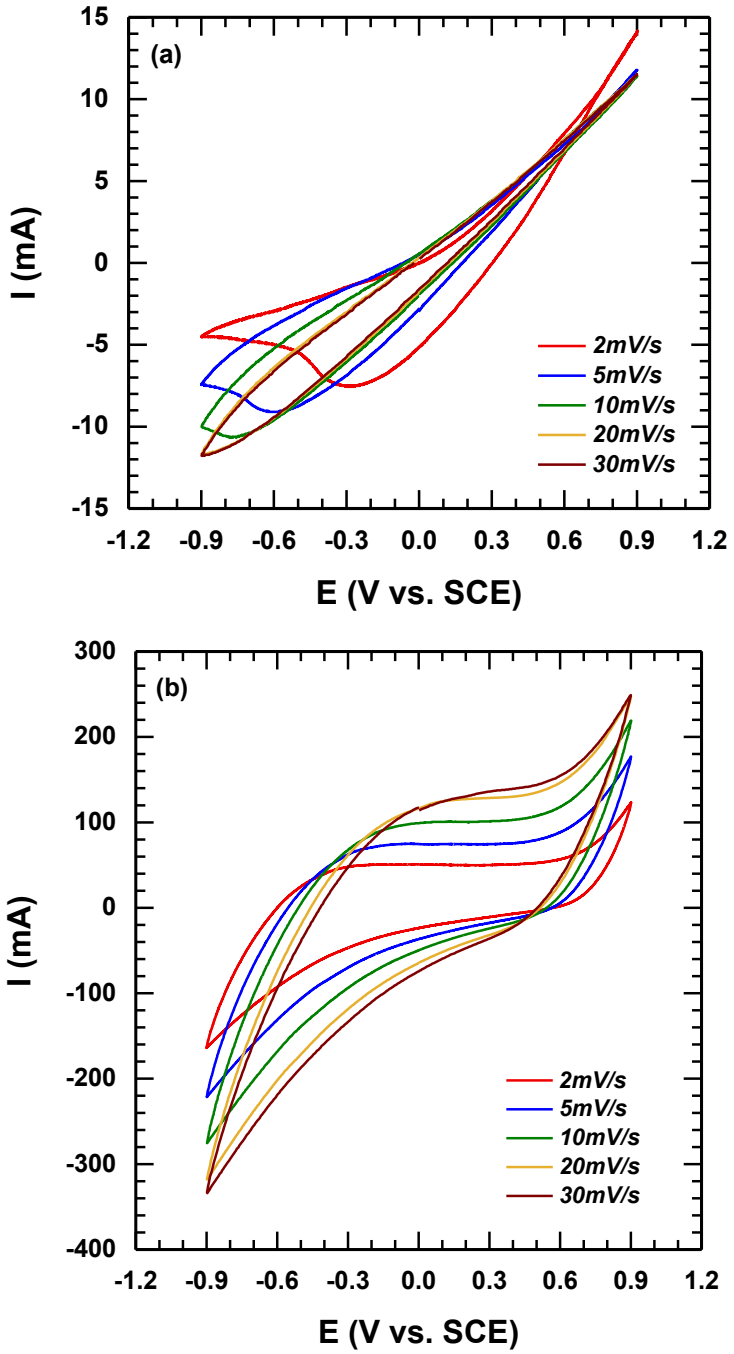

Figure 4.17: CV curve of the NSA/G electrode at different scan rates. Experimental conditions: (a) [NaCl] = 1 mM and (b) 100 mM; effective mass of AC = 0.8 g; pH_i= 6.5

4.3.2 Comparison of Capacitance and Electro-sorption Capacity

The non-faradaic current response from CV scanning in anodic and cathodic direction, brought by the charging of chloride and sodium ions respectively, could represent the capacitance of the electrode. According to eq. (3-5) and eq. (3-6), the anodic (C_a) and cathodic (C_c) instantaneous capacitances can be obtained by separately dividing the anodic (I_a) and cathodic (I_c) current extracted from CV curves by the scan rate. In order to find out some relation between this instantaneous capacitance derived from CV measurements and the actual electro-sorption capacity from direct adsorption experiments in different NaCl concentrations, instantaneous capacitance as a function of applied potential was plotted in Fig. 4.18 and 4.20 (b) and the data are summarized into Table 4.9 and for caparison.

Low NaCl concentration

For predicting ion adsorption density in the batch electro-sorption experiment in 1mM NaCl solution, CV was conducted in the same concentration which is much lower than it generally made for specific capacitance measurements. Fig. 4.18 shows the value of C_a and $-C_c$ as a function of applied potential at different scan rates in 1mM NaCl solution. The instantaneous capacitance increases as decreasing the scan rates which can be attributed to the more effective diffusion of the electrolyte ions into micropores at the low scan rate. The cathodic instantaneous capacitance ($-C_c$) with a negative sign indicating the capacitive charging of sodium ions at 2mV/s was thus chosen to compare with sodium adsorption density from direct electro-sorption. The values of $-C_c$ at given potential were listed in Table 4.9 for comparison.

Next, the values of instantaneous capacitance were converted into capacitive charge density in order to compare with the sodium adsorption density obtained from electro-sorption experiments. The converted capacitive charge density was calculated

from multiplying instantaneous capacitance by the applied potential as shown in the following equation [82],

$$\sigma = CV \tag{4-29}$$

where σ (C/g) is the capacitive charge density accumulated on the single NSA/G electrode; C (F/g) is the instantaneous capacitance of the electrode measured using CV tests; V (Volt) is the applied potential to the three electrode system. Table 4.9 compares the calculated capacitive charge density from CV curves and direct sodium adsorption density from electro-sorption in 1mM NaCl solution at pH 6.5. As can be seen, the values of capacitive charge density are much smaller than the direct sodium adsorption density especially at negative applied potentials.

Based on electrocapillary theory, another method to calculate capacitive charge density is to integrate the instantaneous capacitance derived from CV curves by using eq. (2-11). Fig. 4.19 (a) shows the integral of instantaneous capacitance, that is the charge density on the surface of NSA/G electrode as a function of potential (red line). Assuming that charge density obtained from capacitance is utilized to adsorb electrolyte ions from the solution and E_{pzc} is the potential at the intersection of $-C_c$ curve and C_a curve, a negative sign was added to the red line on the left of E_{pzc} resulting in the blue line in Fig. 4.19 (a). Therefore, the blue line indicates capacitive charge density of Na^+ adsorbed on the NSA/G electrode and can compare with the sodium adsorption density shown in Fig. 4.19 (c).

Similarly, the highest value of capacitive charge density derived from CV is about 3 C/g which is much lower than 15 C/g obtained from the direct adsorption at the potential of -0.7 V (vs. SCE). The calculated charge density from CV in 1mM NaCl is too less to represent the direct electro-sorption of sodium ions in the same solution.

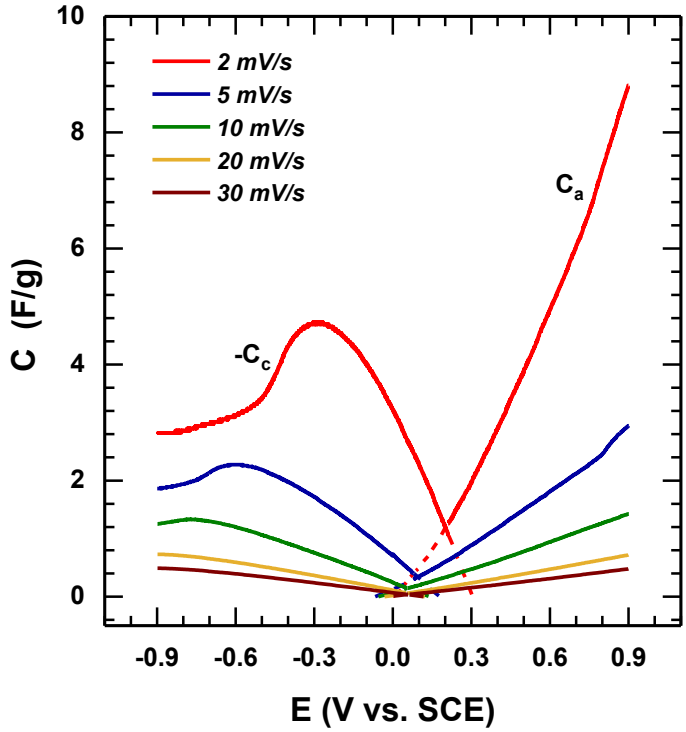

Figure 4.18: Instantaneous capacitance of the NSA/G electrode at different scan rates. Experimental conditions: [NaCl] = 1 mM; effective mass of AC = 0.8g; pH_i = 6.5

Table 4.9: Comparison of capacitive charge of Na^+ derived from CV at 2mV/s and Na^+ charge stored from 80 min direct sorption in 1mM [NaCl]; pH_i= 6.5

E (V vs. SCE)	CV measurement		Direct sorption
	$-C_c$ (F/g)	σ_{Na+} (C/g)	σ_{Na+} (C/g)
0.21 (E_{pzc})	1.18	-0.25	0.43
0.00	3.20	0.00	3.88
-0.30	4.73	1.42	7.49
-0.50	3.43	1.72	11.07
-0.70	2.98	2.09	15.23

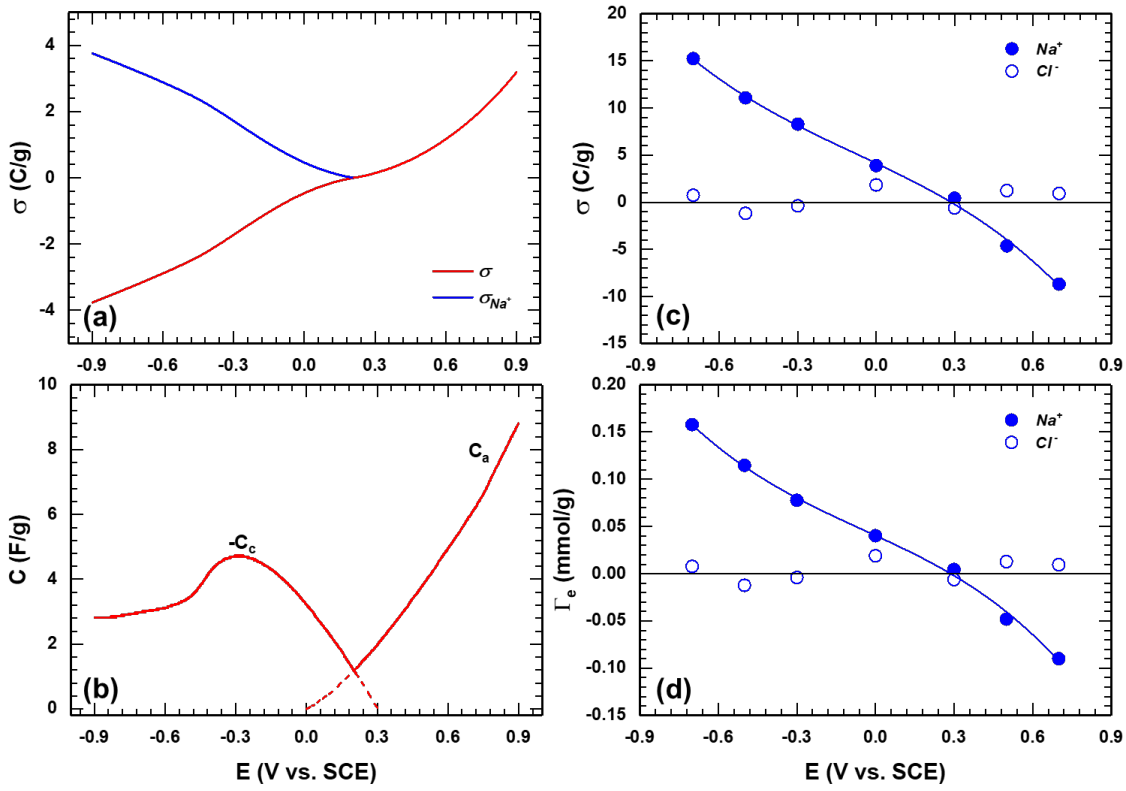

Figure 4.19: (a) Charge density calculated by eq. (2-11) and (b) instantaneous capacitance derived from CV at 2 mV/s; sodium adsorption density in the unit of (c) C/g and (d) mmol/g obtained from direct electro-sorption for 80 min by using the NSA/G electrode. Experimental conditions: [NaCl] = 1 mM; effective mass of AC = 0.8g; pH_i = 6.5

High NaCl concentration

Since the value of capacitive charge density derived from CV is only about a quarter of that obtained from the direct adsorption CV measurements in low NaCl concentration (1mM), it cannot estimate the sodium adsorption in the electro-sorption process very well. Here we run CV in higher NaCl concentrations which are similar to general CV operations. In order to realize the relation between instantaneous capacitance and electrolyte concentration in CV measurements, the CV scanned in different concentrations at 2mV/s under pH 6.5 was performed in Fig. 4.20 (a). The instantaneous capacitance calculated from the CV curve in different concentrations is shown in Fig. 4.20 (b). Dash lines in Fig. 4.20 stand for instantaneous capacitances below E_{pzc} which are not taken into account here.

According to electrocapillary theory, instantaneous capacitance can be integrated into charge density on the surface of electrode by applying eq. (2-11). Thus the surface charge density on NSA/G electrode in different NaCl concentrations is converted from Fig. 4.20 (b) into Fig. 4.21 (a). We assume that charge density integrated from $-C_c$ are all utilized to adsorb and remove sodium ions in the solution. As such, the cathodic charge density in Fig. 4.21 (a) can reflect the amount of adsorbed sodium charge density on the electrode. This part of cathodic charge density was thus added a negative sign and flipped along x-axis to compare with the direct sodium adsorption density in 1mM NaCl solution (blue solid dots) which is shown in Fig. 4.21 (b).

Although the data points for direct sodium adsorption in 1mM NaCl do not overlap with any curve derived from CV in different concentrations completely, they have the same trend and are within same order of magnitude especially with the concentration of 10 mM. In addition, the discrepancy between the estimated sodium

charge density form CV and those from direct sorption should be due to different adsorption time periods applied in each measurement. The hollow dots represent the sodium charge density adsorbed for 2 to 40 min in the same experimental set up as the solid dot at -0.3 V. The hollow dot of 2 min overlaps with 1mM curve derived from CV well which implies the adsorption of sodium ions happened in a very short time period in CV at -0.3 V with less amount of sodium ions be adsorbed. As increasing the adsorption time in direct electro-sorption, the hollow dots move up showing larger sodium charge density. Therefore, the amount of sodium charge density depends on the adsorption time applied. The time parameter needs to be considered when predicting sodium adsorption through any method.

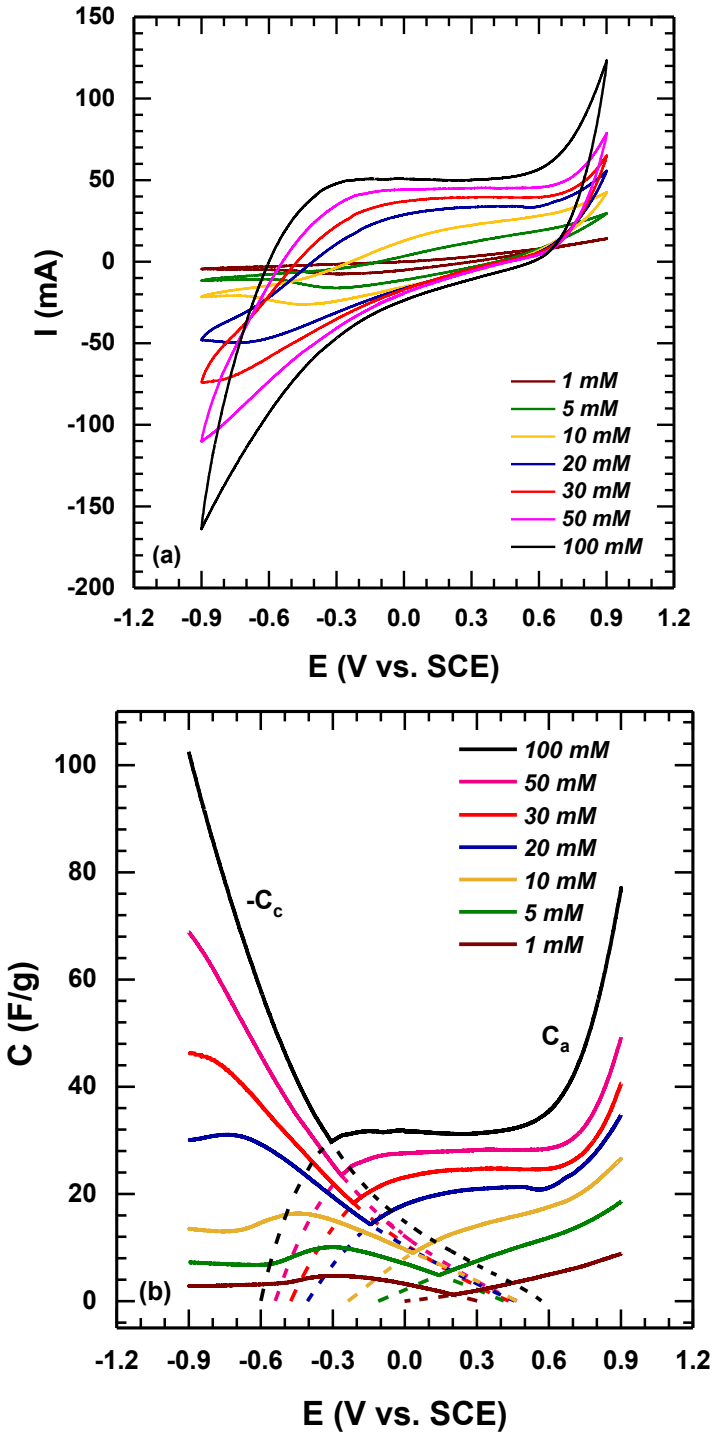

Figure 4.20: (a) CV and (b) instantaneous capacitance of the NSA/G electrode in different NaCl concentrations. Experimental conditions: scan rate = 2mV/s; effective mass of AC = 0.8 g; pH_i= 6.5

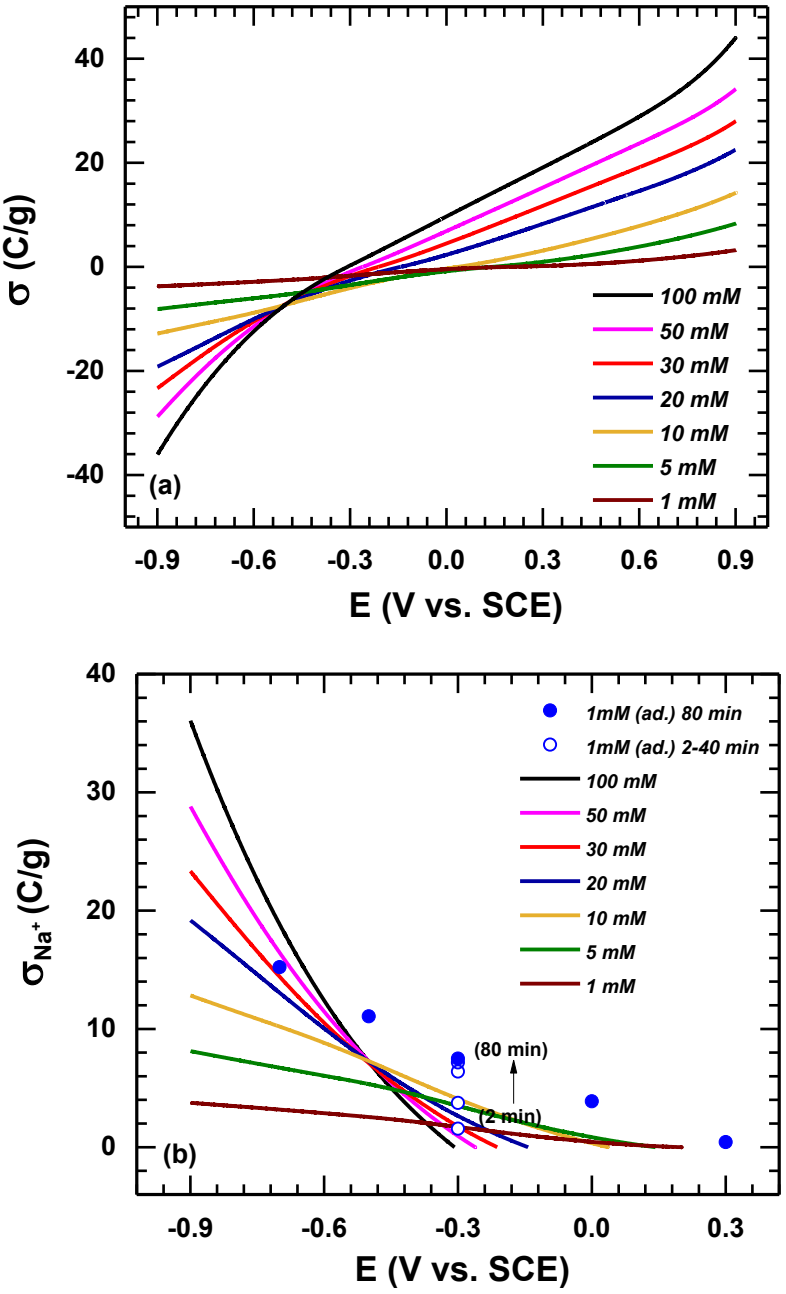

Figure 4.21: (a) Surface charge density and (b) Sodium charge density on the NSA/G electrode both derived from CV in different NaCl concentrations. Experimental conditions: scan rate = 2mV/s; effective mass of AC = 0.8 g; pH_i= 6.5. Blue dots in (b) show adsorbed sodium charge density from 80 min electro-sorption in 1mM NaCl by NSA/G

Capacitance calculated by different methods mentioned in section 3.2.3 in different NaCl concentrations are shown in Fig. 4.22 (a). Data of the point method at E_{pzc} and -0.3 V are obtained from values of instantaneous capacitance at -0.3 V and E_{pzc} under different concentrations in Fig. 4.20 (b). Data from the area method is the average capacitance calculated from the area between CV curves within -0.7 V to +0.7 V (vs. SCE) in different concentrations by the following equation:

$$C = \frac{\oint I\, dV}{2mv\Delta V} \tag{4-30}$$

Results of Fig. 4.22 (a) show the values of cathodic capacitance derived from three different ways are similar and have the same trend. The capacitance calculated from CV area is less than the instantaneous capacitance transformed directly from the current in CV by the other two methods. Furthermore, the values of instantaneous capacitance at -0.3 V from CV calculated by point method was compared to the sodium charge density obtained from direct electro-sorption for 80 min and 10 min showing in Fig 4.22 (b). As can be seen, sodium charge density collected from direct electro-sorption for 80 min is a lot greater than the instantaneous capacitance calculated from CV. However, sodium charge density for 10 min electro-sorption fitted by Freundlich isotherm model is much closer to the instantaneous capacitance data derived from CV. Since there is a multiple around 0.3 between the unit of $-C_c$ (F/g) and that of σ_{Na+} (C/g) according to eq. (4-29), σ_{Na+} converted from the instantaneous capacitance of CV under -0.3 V is actually about 0.3 times of that obtained from the 10 min electro-sorption. This difference should mainly result from the different time periods applied in CV measurements and direct adsorption experiments.

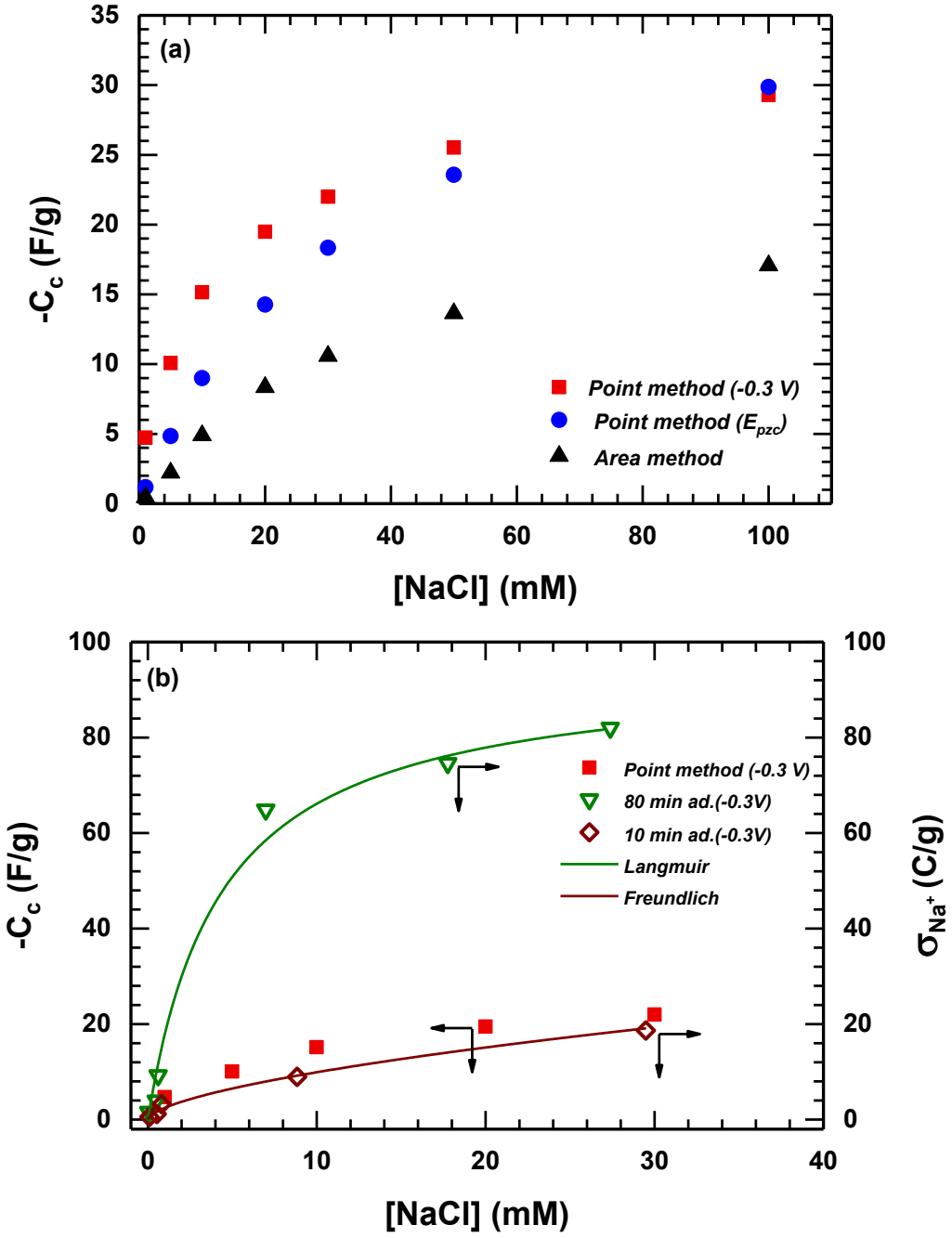

Figure 4.22: (a) Cathodic capacitance calculated by different methods from CV and (b) Sodium charge density collected from direct electro-sorption for 80 min and 10 min at different NaCl concentrations. Data fitted by different isotherm models and compared with (a). Experimental conditions: scan rate = 2mV/s; effective mass of AC = 0.8 g; pH_i= 6.5

For CV measurements, the cathodic capacitive current responding at -0.3 V happened immediately within only seconds. Plus, the adsorption of sodium ions as a function of time has maximum slope at the beginning of electro-sorption experiment which can be seen in Fig. 4.9. This illustrates that the adsorption rate is the fastest when first start and becomes slower over time. Thus the instantaneous capacitance and charge density calculated from CV are representing sodium adsorption at the very beginning time of the electro-sorption with the fastest adsorption rate.

However, for direct adsorption experiments, the result of sodium adsorption density is the total adsorbed sodium ions in NaCl solution over 80 (or 10) minutes. The number of sodium adsorption density should depend on how long the electro-sorption was conducted. This is true because sodium adsorption density from electro-sorption for 80 min is larger than that for 10 min and both of which are much larger than the sodium charge density measured in CV for only seconds.

To conclude, CV measures charge density at a certain voltage in a short time period while electro-sorption shows total adsorbed charge density under a fix applied voltage in a long time period. Time period should be taken into account when applying CV method to predict ion adsorption density from electro-sorption process. In spite of the discrepancy between CV method and the electro-sorption process, the trend of instantaneous capacitance derived from CV can still be fitted with Freundlich isotherm model very well. In addition, there is a ratio around 0.3:1 between sodium charge density calculated from CV and that from 10 min electro-sorption process in different concentrations which could be further used to predict sodium adsorption density of electro-sorption processes within same time period for other concentrations.

Chapter 5

MAJOR FINDINGS AND FUTURE RESEARCH

5.1 Major Findings

Two kinds of commercial activated carbon were supported on graphite sheet to prepare electrodes for electro-sorption of sodium chloride in dilute aqueous solutions. Surface characterization showed high BET surface area of 1732.63 m^2/g and 802.36 m^2/g for NSA AC and F400 AC, respectively. The ratio of AC: PVDF (4:1) for electrode preparation can be confirmed in the SEM-EDX spectra. Results of X-ray analysis showed the chemical states of C and O on the surface and that both ACs are less-crystalline porous solids. Zeta potential measurements indicated the pH_{pzc} of NSA AC and F400 AC are around 3 and 6, respectively.

This study investigated the capacitive properties during electro-sorption of sodium chloride by the NSA/G electrode and left that part of F400/G electrode for future work. Results revealed conductivity measurements for determining NaCl removal is not accurate since the assumption of symmetric adsorption of anions and cations is not always true and that conductivity values will be affected by other ions like H^+ and OH^- in the solution. Thus, individual concentrations of sodium and chloride ions had been analyzed by IC to evaluate the actual NaCl removal. Based on the results of much higher adsorption on sodium ions than chlorides ions by the NSA/G electrode in NaCl solutions, further analysis on sodium electro-sorption under different electrolyte conditions were done. Results showed Langmuir and Freundlich models are best applicable to the adsorption isotherms of Na^+ by the NSA/G electrode for 80 min and 10 min adsorption,

respectively. Also, the electro-sorption and desorption of Na^+ onto the NSA/G electrode follow the pseudo-first-order rate model very well in 1mM NaCl.

Sodium adsorption densities by the NSA/G electrode were analyzed in terms of electrical double layer whose charging mechanisms were composed of polarizable and reversible interfaces. Therefore, the electro-sorption data were examined through two important factors, applied potential and solution pH which have showed obvious influence on sodium removal. Along with the aid of Gouy-Chapman theory, the adsorbed sodium charge densities contributed from both potential effect and pH effect can be estimated. And the difference between the theoretically predicted sodium charge density and the actual values may possible due to NSA/G electrode as a capacitor was not absolutely charged.

Cyclic voltammetry showed the electrochemical characteristics of NSA/G electrode performing in the same conditions as in the electro-sorption process. Owing to different time periods applied between CV measurements and electro-sorption processes on sodium adsorption, a higher electrolyte concentration (e.g. 10 mM) in CV is essential to estimate the adsorbed sodium charge density from 80 min electro-sorption in lower NaCl concentration (e.g. 1mM). However, a ratio around 0.3:1 of the sodium charge density obtained from CV to that measured from 10 min electro-sorption at the same applied potential is successfully derived. Overall, results demonstrated that potential and pH effects both play important roles on ion electro-sorption and CV method is a feasible way in estimating Na^+ adsorption density by NSA/G electrode.

5.2 Future Research Needs

Results of the present study demonstrated the design of NSA/G electrode with negatively-charged surface to electrochemically adsorbed sodium and chloride ions under different pH conditions. It was found that NSA/G electrode asymmetrically adsorbed anions and cations and that direct measurement of ion removal was more accurate than indirect conductivity measurement when assessing CDI removal of NaCl from aqueous solutions. Thus, we suggest to determine NaCl removal by analyzing the concentrations of individual species in solution by IC or other ion analytical instruments in future CDI studies.

Besides, results showed externally applied potential and pH were both important factors on sodium electro-sorption by NSA/G electrode. Therefore, F400/G electrode with positively-charged surface should favor adsorption of anions. A series of sodium and chloride electro-sorption experiments need to be compared by F400/G electrode in the future. In order to verify the hypothesis that NaCl removal will be greatly enhanced by incorporating F400 as a high pH_{pzc} AC on the anode and NSA as a low pH_{pzc} AC on the cathode in a specific pH range, an asymmetric electrochemical cell assembled by NSA/G and F400/G electrodes can be tested in two-electrode system as to compare the performance of other CDI cells on the electro-sorption of ions.

Lastly, the instantaneous capacitance of electrodes at a certain potential estimated by CV measurement is more accurate and practical than the average capacitance calculated by the area method which has been applied in most literature. By exploiting point method with an expected capacitance, we can predict the voltage needed to apply in electro-sorption when designing experiments in the future.

REFERENCES

[1] F. A.AlMarzooqi, A. A.AlGhaferi, I.Saadat, andN.Hilal, "Application of Capacitive Deionisation in water desalination: A review," *Desalination*, vol. 342, pp. 3–15, 2014.

[2] A. D.Khawaji, I. K.Kutubkhanah, andJ. M.Wie, "Advances in seawater desalination technologies," *Desalination*, vol. 221, no. 1–3, pp. 47–69, 2008.

[3] M. A.Ahmed andS.Tewari, "Capacitive deionization: Processes, materials and state of the technology," *J. Electroanal. Chem.*, vol. 813, pp. 178–192, 2018.

[4] J.Choi, P.Dorji, H. K.Shon, andS.Hong, "Applications of capacitive deionization: Desalination, softening, selective removal, and energy efficiency," *Desalination*, vol. 468, no. June 2018, pp. 118–130, 2019.

[5] S. J.Seo *et al.*, "Investigation on removal of hardness ions by capacitive deionization (CDI) for water softening applications," *Water Res.*, vol. 44, no. 7, pp. 2267–2275, 2010.

[6] Y. J.Shih, C.DiDong, Y. H.Huang, andC. P.Huang, "Electro-sorption of ammonium ion onto nickel foam supported highly microporous activated carbon prepared from agricultural residues (dried Luffa cylindrica)," *Sci. Total Environ.*, vol. 673, pp. 296–305, 2019.

[7] W.Stumm, C.Huang, andS.Jenkins, "Specific Chemical Interaction Affecting the Stability of Dispersed Systems," *Croat. Chem. Acta*, vol. 42, no. 2, pp. 223–245, 1970.

[8] C. P.Huang, *THE ELECTRICAL DOUBLE LAYER OF γ−Al2O3 - ELECTROLYTE SYSTEM*. ACADEMIC PRESS, INC., 1976.

[9] M. O.Corapcioglu andC. P.Huang, "The surface acidity and characterization of some commercial activated carbons," *Carbon N. Y.*, vol. 25, no. 4, pp. 569–578, 1987.

[10] R. L.Zornitta, J. J.Lado, M. A.Anderson, andL. A. M.Ruotolo, "Effect of electrode properties and operational parameters on capacitive deionization using low-cost commercial carbons," *Sep. Purif. Technol.*, vol. 158, pp. 39–52, 2016.

[11] H.Li, L.Zou, L.Pan, andZ.Sun, “Novel graphene-like electrodes for capacitive deionization,” *Environ. Sci. Technol.*, vol. 44, no. 22, pp. 8692–8697, 2010.

[12] H. J.Oh, J. H.Lee, H. J.Ahn, Y.Jeong, Y. J.Kim, andC. S.Chi, “Nanoporous activated carbon cloth for capacitive deionization of aqueous solution,” *Thin Solid Films*, vol. 515, no. 1, pp. 220–225, 2006.

[13] M. A.Anderson, A. L.Cudero, andJ.Palma, “Capacitive deionization as an electrochemical means of saving energy and delivering clean water. Comparison to present desalination practices: Will it compete?,” *Electrochim. Acta*, vol. 55, no. 12, pp. 3845–3856, 2010.

[14] M. E.Suss, S.Porada, X.Sun, P. M.Biesheuvel, J.Yoon, andV.Presser, “Water desalination via capacitive deionization: What is it and what can we expect from it?,” *Energy Environ. Sci.*, vol. 8, no. 8, pp. 2296–2319, 2015.

[15] S.Porada, R.Zhao, A.Van DerWal, V.Presser, andP. M.Biesheuvel, “Review on the science and technology of water desalination by capacitive deionization,” *Prog. Mater. Sci.*, vol. 58, no. 8, pp. 1388–1442, 2013.

[16] J. Y.Lee, S. J.Seo, S. H.Yun, andS. H.Moon, “Preparation of ion exchanger layered electrodes for advanced membrane capacitive deionization (MCDI),” *Water Res.*, vol. 45, no. 17, pp. 5375–5380, 2011.

[17] H.Li andL.Zou, “Ion-exchange membrane capacitive deionization: A new strategy for brackish water desalination,” *Desalination*, vol. 275, no. 1–3, pp. 62–66, 2011.

[18] L.Wang *et al.*, “Capacitive deionization of NaCl solutions using carbon nanotube sponge electrodes,” *J. Mater. Chem.*, vol. 21, no. 45, pp. 18295–18299, 2011.

[19] S.IlJeon *et al.*, “Desalination via a new membrane capacitive deionization process utilizing flow-electrodes,” *Energy Environ. Sci.*, vol. 6, no. 5, pp. 1471–1475, 2013.

[20] J.Lee, S.Kim, C.Kim, andJ.Yoon, “Hybrid capacitive deionization to enhance the desalination performance of capacitive techniques,” *Energy Environ. Sci.*, vol. 7, no. 11, pp. 3683–3689, 2014.

[21] X.Gao, A.Omosebi, J.Landon, andK.Liu, “Surface charge enhanced carbon electrodes for stable and efficient capacitive deionization using inverted adsorption-desorption behavior,” *Energy Environ. Sci.*, vol. 8, no. 3, pp. 897–909, 2015.

[22] Y. W.Chen, J. F.Chen, C. H.Lin, andC. H.Hou, “Integrating a supercapacitor with capacitive deionization for direct energy recovery from the desalination of brackish water,” *Appl. Energy*, vol. 252, no. May, 2019.

[23] P. M.Biesheuvel, R.Zhao, S.Porada, andA.van derWal, “Theory of membrane capacitive deionization including the effect of the electrode pore space,” *J. Colloid Interface Sci.*, vol. 360, no. 1, pp. 239–248, 2011.

[24] Y. A. C.Jande andW. S.Kim, “Desalination using capacitive deionization at constant current,” *Desalination*, vol. 329, pp. 29–34, 2013.

[25] S.IlJeon, J. G.Yeo, S.Yang, J.Choi, andD. K.Kim, “Ion storage and energy recovery of a flow-electrode capacitive deionization process,” *J. Mater. Chem. A*, vol. 2, no. 18, pp. 6378–6383, 2014.

[26] Y.Oren, “Capacitive deionization (CDI) for desalination and water treatment - past, present and future (a review),” *Desalination*, vol. 228, no. 1–3, pp. 10–29, 2008.

[27] H. J.Ahn, J. H.Lee, Y.Jeong, J. H.Lee, C. S.Chi, andH. J.Oh, “Nanostructured carbon cloth electrode for desalination from aqueous solutions,” *Mater. Sci. Eng. A*, vol. 448–451, pp. 841–845, 2007.

[28] E.Ayranci andB. E.Conway, “Adsorption and electrosorption at high-area carbon-felt electrodes for waste-water purification: Systems evaluation with inorganic, S-containing anions,” *J. Appl. Electrochem.*, vol. 31, no. 3, pp. 257–266, 2001.

[29] S.Nadakatti, M.Tendulkar, andM.Kadam, “Use of mesoporous conductive carbon black to enhance performance of activated carbon electrodes in capacitive deionization technology,” *Desalination*, vol. 268, no. 1–3, pp. 182–188, 2011.

[30] Y.Gao *et al.*, “Electrosorption behavior of cations with carbon nanotubes and carbon nanofibres composite film electrodes,” *Thin Solid Films*, vol. 517, no. 5, pp. 1616–1619, 2009.

[31] X. Z.Wang *et al.*, “Electrosorption of ions from aqueous solutions with carbon nanotubes and nanofibers composite film electrodes,” *Appl. Phys. Lett.*, vol. 89, no. 5, pp. 87–90, 2006.

[32] A.Aghigh, V.Alizadeh, H. Y.Wong, M. S.Islam, N.Amin, andM.Zaman, “Recent advances in utilization of graphene for filtration and desalination of water: A review,” *Desalination*, vol. 365, pp. 389–397, 2015.

[33] F.Perreault, A.Fonseca De Faria, andM.Elimelech, “Environmental applications of graphene-based nanomaterials,” *Chem. Soc. Rev.*, vol. 44, no. 16, pp. 5861–5896, 2015.

[34] L.Zou, L.Li, H.Song, andG.Morris, “Using mesoporous carbon electrodes for brackish water desalination,” *Water Res.*, vol. 42, no. 8–9, pp. 2340–2348, 2008.

[35] L.Li, L.Zou, H.Song, andG.Morris, “Ordered mesoporous carbons synthesized by a modified sol-gel process for electrosorptive removal of sodium chloride,” *Carbon N. Y.*, vol. 47, no. 3, pp. 775–781, 2009.

[36] C. L.Yeh, H. C.Hsi, K. C.Li, andC. H.Hou, “Improved performance in capacitive deionization of activated carbon electrodes with a tunable mesopore and micropore ratio,” *Desalination*, vol. 367, pp. 60–68, 2015.

[37] D. C.Grahame, “The electrical double layer and the theory of electrocapillarity,” *Chem. Rev.*, vol. 41, no. 3, pp. 441–501, 1947.

[38] B. E.Conway, J. O. M.Bockris, andI. A.Ammar, “The dielectric constant of the solution in the diffuse and Helmholtz double layers at a charged interface in aqueous solution,” *Trans. Faraday Soc.*, vol. 47, pp. 756–766, 1951.

[39] A. J.Bard, L. R.Faulkner, J.Leddy, andC. G.Zoski, *Electrochemical methods: fundamentals and applications*, vol. 2. 1980.

[40] M. G.Lippmann, “Relations entre les phénomènes électriques et capillaires,” *Ann. Chim. Phys.*, vol. 5, no. 28. p. 494, 1875.

[41] A.Frumkin, O.Petry, andB.Damaskin, “The Notion of the Electrode Charge and the Lippmann Equation,” vol. 27, pp. 81–100, 1970.

[42] P. C.Hiemenz andE.Raj Rajagopalan, *Principles of Colloid and Surface Chemistry, revised and expanded*. CRC press, 2016.

[43] X.Ning, W.Zhong, S.Li, Y.Wangb, andW.Yangb, “High performance nitrogen-doped porous graphene/carbon frameworks for supercapacitors,” *J. Mater. Chem. A*, pp. 8859–8867, 2014.

[44] A. S.Yasin, M.Obaid, I. M. A.Mohamed, A.Yousef, andN. A. M.Barakat, “ZrO2 nanofibers/activated carbon composite as a novel and effective electrode material for the enhancement of capacitive deionization performance,” *RSC Adv.*, vol. 7, no. 8, pp. 4616–4626, 2017.

[45] R.Mahmudov andC. P.Huang, “Perchlorate removal by activated carbon adsorption,” *Sep. Purif. Technol.*, vol. 70, no. 3, pp. 329–337, 2010.

[46] A.Kumar andH. M.Jena, “Preparation and characterization of high surface area activated carbon from Fox nut (Euryale ferox) shell by chemical activation with H3PO4,” *Results Phys.*, vol. 6, pp. 651–658, 2016.

[47] Q.Lu andG. A.Sorial, “Adsorption of phenolics on activated carbon — impact of pore size and molecular oxygen,” vol. 55, pp. 671–679, 2004.

[48] N.Yoshizawa, Y.Yamada, M.Shiraishi, K.Kaneko, andN.Setoyamab, “Evaluation of accessible and inaccessible microporosities of microporous carbons,” vol. 92, no. 12, pp. 2297–2302, 1996.

[49] B.Singh, Y.Fang, B. C. C.Cowie, andL.Thomsen, “NEXAFS and XPS characterisation of carbon functional groups of fresh and aged biochars,” *Org. Geochem.*, vol. 77, pp. 1–10, 2014.

[50] Y. C.Chiang, W. H.Lin, andY. C.Chang, “The influence of treatment duration on multi-walled carbon nanotubes functionalized by H 2 SO 4 /HNO 3 oxidation,” *Appl. Surf. Sci.*, vol. 257, no. 6, pp. 2401–2410, 2011.

[51] M.Adib, Z.Al-qodah, andC. W. Z.Ngah, “Agricultural bio-waste materials as potential sustainable precursors used for activated carbon production : A review,” *Renew. Sustain. Energy Rev.*, vol. 46, pp. 218–235, 2015.

[52] Z.Zheng, J.Kemeny, andN. G. W.Cook, “THE REMOVAL OF CHROMIUM(VI) FROM DILUTE AQUEOUS SOLUTION BY ACTIVATED CARBON,” vol. 94, no. 88, pp. 7171–7182, 1989.

[53] T.Wu *et al.*, “Surface-treated carbon electrodes with modified potential of zero charge for capacitive deionization,” *Water Res.*, vol. 93, pp. 30–37, 2016.

[54] Y. J.Kim andJ. H.Choi, “Enhanced desalination efficiency in capacitive deionization with an ion-selective membrane,” *Sep. Purif. Technol.*, vol. 71, no. 1, pp. 70–75, 2010.

[55] R. L.Zornitta andL. A. M.Ruotolo, “Simultaneous analysis of electrosorption capacity and kinetics for CDI desalination using different electrode configurations,” *Chem. Eng. J.*, vol. 332, no. September 2017, pp. 33–41, 2018.

[56] X.Gao *et al.*, “Polymer-coated composite anodes for efficient and stable capacitive deionization,” *Desalination*, vol. 399, pp. 16–20, 2016.

[57] T.Wu *et al.*, “Starch Derived Porous Carbon Nanosheets for High-Performance Photovoltaic Capacitive Deionization,” *Environ. Sci. Technol.*, vol. 51, no. 16, pp. 9244–9251, 2017.

[58] W.Li, L.Lei, Z.Yun, andF.Jiangtao, “Fabrication of titanium carburizing electrodes for capacitive deionization,” *Water Sci. Technol.*, vol. 76, no. 4, pp. 754–760, 2017.

[59] M. S.Zoromba, M. H.Abdel-Aziz, M.Bassyouni, S.Gutub, D.Demko, andA.Abdelkader, “Electrochemical Activation of Graphene at Low Temperature: The Synthesis of Three-Dimensional Nanoarchitectures for High Performance Supercapacitors and Capacitive Deionization,” *ACS Sustain. Chem. Eng.*, vol. 5, no. 6, pp. 4573–4581, 2017.

[60] Y.Li *et al.*, “Nitrogen-Doped Hollow Mesoporous Carbon Spheres for Efficient Water Desalination by Capacitive Deionization,” *ACS Sustain. Chem. Eng.*, vol. 5, no. 8, pp. 6635–6644, 2017.

[61] Y. C.Tsai andR. anDoong, “Hierarchically ordered mesoporous carbons and silver nanoparticles as asymmetric electrodes for highly efficient capacitive deionization,” *Desalination*, vol. 398, pp. 171–179, 2016.

[62] M. W.Ryoo andG.Seo, “Improvement in capacitive deionization function of activated carbon cloth by titania modification,” *Water Res.*, vol. 37, no. 7, pp. 1527–1534, 2003.

[63] X. Z.Wang *et al.*, “Electrosorption of ions from aqueous solutions with carbon nanotubes and nanofibers composite film electrodes,” *Appl. Phys. Lett.*, vol. 89, no. 5, 2006.

[64] S. J.Seo *et al.*, “Investigation on removal of hardness ions by capacitive deionization (CDI) for water softening applications,” *Water Res.*, vol. 44, no. 7, pp. 2267–2275, 2010.

[65] K. C.Leonard, J. R.Genthe, J. L.Sanfilippo, W. A.Zeltner, andM. A.Anderson, “Synthesis and characterization of asymmetric electrochemical capacitive deionization materials using nanoporous silicon dioxide and magnesium doped aluminum oxide,” *Electrochim. Acta*, vol. 54, no. 22, pp. 5286–5291, 2009.

[66] Z.Chen, H.Zhang, C.Wu, Y.Wang, andW.Li, “A study of electrosorption selectivity of anions by activated carbon electrodes in capacitive deionization,” *Desalination*, vol. 369, pp. 46–50, 2015.

[67] C. J.Gabelich, T. D.Tran, andI. H.Suffet, “Electrosorption of inorganic salts from aqueous solution using carbon aerogels,” *Environ. Sci. Technol.*, vol. 36, no. 13, pp. 3010–3019, 2002.

[68] W.Cai, J.Yan, T.Hussin, andJ.Liu, “Nafion-AC-based asymmetric capacitive deionization,” *Electrochim. Acta*, vol. 225, pp. 407–415, 2017.

[69] C. H.Fang *et al.*, “A flexible and hydrophobic polyurethane elastomer used as binder for the activated carbon electrode in capacitive deionization,” *Desalination*, vol. 399, pp. 34–39, 2016.

[70] M. R.Matsumoto, “Modeling cadmium adsorption by activated carbon using the langmuir and freundlich isotherm expressions,” *Sep. Sci. Technol.*, vol. 28, no. 13–14, pp. 2179–2195, 1993.

[71] S.Goldberg andG. E.Brown, “Equations and Models Describing Adsorption Processes in Soils,” no. 8, pp. 489–517, 2005.

[72] H. K.Chung, W. H.Kim, J.Park, J.Cho, T. Y.Jeong, andP. K.Park, “Application of Langmuir and Freundlich isotherms to predict adsorbate removal efficiency or required amount of adsorbent,” *J. Ind. Eng. Chem.*, vol. 28, pp. 241–246, 2015.

[73] D.A.O, “Langmuir, Freundlich, Temkin and Dubinin–Radushkevich Isotherms Studies of Equilibrium Sorption of Zn 2+ Unto Phosphoric Acid Modified Rice Husk,” *IOSR J. Appl. Chem.*, vol. 3, no. 1, pp. 38–45, 2012.

[74] G.Bharath *et al.*, “Development of adsorption and electrosorption techniques for removal of organic and inorganic pollutants from wastewater using novel magnetite/porous graphene-based nanocomposites,” *Sep. Purif. Technol.*, vol. 188, pp. 206–218, 2017.

[75] M.Franz, H. A.Arafat, andN. G.Pinto, “Effect of chemical surface heterogeneity on the adsorption mechanism of dissolved aromatics on activated carbon,” *Carbon N. Y.*, vol. 38, no. 13, pp. 1807–1819, 2000.

[76] H.Qiu, L.Lv, B. C.Pan, Q. J.Zhang, W. M.Zhang, andQ. X.Zhang, “Critical review in adsorption kinetic models,” *J. Zhejiang Univ. Sci. A*, vol. 10, no. 5, pp. 716–724, 2009.

[77] Z.Chen, C.Song, X.Sun, H.Guo, andG.Zhu, “Kinetic and isotherm studies on the electrosorption of NaCl from aqueous solutions by activated carbon electrodes,” *Desalination*, vol. 267, no. 2–3, pp. 239–243, 2011.

[78] M.Dogan, H.Abak, andM.Alkan, “Adsorption of methylene blue onto hazelnut shell : Kinetics , mechanism and activation parameters,” vol. 164, pp. 172–181, 2009.

[79] W.Tang, D.He, C.Zhang, P.Kovalsky, andT. D.Waite, “Comparison of Faradaic reactions in capacitive deionization (CDI) and membrane capacitive deionization (MCDI) water treatment processes,” *Water Res.*, vol. 120, pp. 229–237, 2017.

[80] R.Mysyk, E.Raymundo-Piñero, andF.Béguin, “Saturation of subnanometer pores in an electric double-layer capacitor,” *Electrochem. commun.*, vol. 11, no. 3, pp. 554–556, 2009.

[81] N.Elgrishi, K. J.Rountree, B. D.McCarthy, E. S.Rountree, T. T.Eisenhart, andJ. L.Dempsey, “A Practical Beginner’s Guide to Cyclic Voltammetry,” *J. Chem. Educ.*, vol. 95, no. 2, pp. 197–206, 2018.

[82] T.Kim andJ.Yoon, “Relationship between capacitance of activated carbon composite electrodes measured at a low electrolyte concentration and their desalination performance in capacitive deionization,” *J. Electroanal. Chem.*, vol. 704, pp. 169–174, 2013.

Appendix

SUPPORTING INORMATION

Table A.1: Plotting data for Fig. 4.5

NSA AC						F400 AC					
0.01M		0.05M		0.1M		0.01M		0.05M		0.1M	
pH_f	ζ (mV)	pH_f	ζ (mV)	pH_f	ζ (mV)	pH_f	ζ (mV)	pH_f	ζ (mV)	pH_f	ζ (mV)
9.89	-24.83	10.67	-19.30	11.10	-15.90	1.24	7.10	1.23	5.45	1.34	6.22
8.34	-26.07	10.01	-20.80	9.65	-16.93	2.15	7.79	2.16	6.83	3.17	-0.02
6.72	-26.13	8.75	-18.90	7.07	-12.20	3.18	5.54	3.01	6.17	4.26	-2.08
4.60	-20.20	6.61	-13.93	5.67	-13.23	4.59	3.15	4.40	0.45	5.17	-2.17
4.05	-19.07	4.94	-13.10	3.72	-6.29	4.97	2.41	5.45	-3.89	5.83	-5.98
3.39	-14.07	4.00	-9.18	2.79	-5.41	5.28	-2.10	6.12	-4.83	5.60	-3.71
2.75	-4.13	3.04	-6.24	2.05	-2.07	6.00	-11.80	6.50	-9.39	6.84	-14.30
2.14	-0.86	2.59	-3.56	1.77	-0.88	6.64	-13.40	6.95	-9.89	7.53	-10.70
1.96	4.64	2.05	-1.64	1.51	0.25	6.85	-23.50	8.78	-17.20	9.45	-15.30
1.78	9.46	1.78	0.45	1.42	0.41	8.65	-26.40	10.66	-22.10	10.65	-16.80
		1.57	1.13			10.66	-34.80	11.90	-25.30	11.85	-19.40
		1.45	1.34			11.99	-42.50	7.56	-10.30		
		1.06	1.61			6.32	-11.70				

Table A.2: Plotting data for Fig. 4.6

0.1mM		1 mM		10 mM	
Time (min)	C/C_0 (%)	Time (min)	C/C_0 (%)	Time (min)	C/C_0 (%)
0.0	100.0	0.0	100.0	5.0	100.0
2.0	84.8	2.0	94.4	10.0	96.7
5.0	82.7	5.0	86.5	20.0	92.3
10.0	83.0	10.0	88.3	40.0	81.1
20.0	73.1	20.0	76.9	60.0	84.5
40.0	58.3	40.0	74.1	80.0	76.5
80.0	54.4	80.0	66.6	85.0	94.0
85.0	63.2	90.0	76.4	90.0	96.5
90.0	69.6	100.0	82.6	100.0	93.7
100.0	71.7	160.0	91.8	120.0	93.2
120.0	88.7			160.0	94.9
160.0	92.2				

Table A.3: Plotting data for Fig. 4.7 (a) and (b)

Fig. 4.7 (a)				Fig. 4.7 (b)			
80 min		10 min		80 min		10 min	
Γ_e (mmol/g)	C_e (mM)	Γ_e (mmol/g)	C_e (mM)	Γ_e (mmol/g)	C_e/Γ_e (g/L)	Γ_e (mmol/g)	C_e/Γ_e (g/L)
0.02	0.06	0.01	0.10	0.02	0.06	0.01	15.66
0.04	0.50	0.01	0.53	0.04	0.50	0.01	43.26
0.10	0.61	0.03	0.81	0.10	0.61	0.03	24.23
0.67	6.99	0.09	8.84	0.67	6.99	0.09	95.24
0.77	17.76	0.19	29.48	0.77	17.76	0.19	152.39
0.85	27.38			0.85	27.38		

Table A.4: Plotting data for Fig. 4.9

Time (min)	Γ_t (mmol/g)	Time (min)	Γ_t (mmol/g)	Time (min)	Γ_t (mmol/g)
0	0.000	0	0.000	5	0.000
2	0.005	2	0.016	10	0.093
5	0.006	5	0.039	20	0.219
10	0.006	10	0.033	40	0.541
20	0.010	20	0.066	80	0.672
40	0.015	40	0.074	85	0.171
80	0.016	80	0.096	100	0.181
85	0.016	90	0.068	120	0.194
90	0.013	100	0.050	160	0.145
100	0.011	160	0.024		
120	0.010				
160	0.004				
	0.003				

Table A.5: Plotting data for Fig. 4.10 and Fig. 4.11

pH 3			pH 6.5		pH 10	
$E-E_{pzc}$ (V)	Γ_e (Na^+) (mmol/g)	Γ_e (Cl^-) (mmol/g)	Γ_e (Na^+) (mmol/g)	Γ_e (Cl^-) (mmol/g)	Γ_e (Na^+) (mmol/g)	Γ_e (Cl^-) (mmol/g)
-1	0.055	-0.006	0.158	0.008	0.237	-0.004
-0.8	0.031	0.001	0.115	-0.012	0.206	-0.002
-0.6	0.011	0.002	0.086	-0.004	0.122	-0.022
-0.3	--	0.000	0.040	0.019	0.054	-0.011
0	0.008	0.009	0.004	-0.006	-0.007	0.002
0.2	0.002	0.003	-0.048	0.013	-0.021	-0.024
0.4	-0.002	0.001	-0.090	0.010	-0.151	-0.015

Table A.6: Plotting data for Fig. 4.12 (a) and (b)

Fig. 4.12 (a)				Fig. 4.12 (b)			
$E-E_{pzc}$ (V)	pH 3 Γ_e (mmol/g)	pH 6.5 Γ_e (mmol/g)	pH 10 Γ_e (mmol/g)	$E-E_{pzc}$ (V)	pH 3 σ_{Na+} (C/g)	pH 6.5 σ_{Na+} (C/g)	pH 10 σ_{Na+} (C/g)
-1	0.055	0.158	0.237	-1	5.345	15.229	22.825
-0.8	0.031	0.115	0.206	-0.8	3.008	11.070	19.900
-0.6	0.011	0.086	0.122	-0.6	1.049	8.275	11.816
-0.3	--	0.040	0.054	-0.3	--	3.881	5.181
0	0.008	0.004	-0.007	0	0.762	0.429	-0.710
0.2	0.002	-0.048	-0.021	0.2	0.167	-4.632	-2.030
0.4	-0.002	-0.090	-0.151	0.4	-0.155	-8.679	-14.526

Table A.7: Plotting data for Fig. 4.13 (a)

0.01M				0.05M				0.1M			
pH_f	ζ (mV)	Ψ_0 (mV)	σ_{Na+} ($\mu C/cm^2$)	pH_f	ζ (mV)	Ψ_0 (mV)	σ_{Na+} ($\mu C/cm^2$)	pH_f	ζ (mV)	Ψ_0 (mV)	σ_{Na+} ($\mu C/cm^2$)
11.10	-29.07	-99.67	-4.00	10.67	-19.30	-57.06	-1.59	11.10	-15.90	-45.65	-1.18
7.31	-27.60	-91.72	-3.40	10.01	-20.80	-62.47	-1.80	9.65	-16.93	-49.01	-1.30
6.75	-25.17	-80.12	-2.67	8.75	-18.90	-55.66	-1.53	7.07	-12.20	-34.21	-0.84
4.64	-15.60	-44.69	-1.15	6.61	-13.93	-39.47	-0.99	5.67	-13.23	-37.33	-0.93
4.02	-12.77	-35.92	-0.89	4.94	-13.10	-36.92	-0.92	3.72	-6.29	-17.23	-0.40
3.37	-11.27	-31.45	-0.76	4.00	-9.18	-25.40	-0.60	2.79	-5.41	-14.78	-0.34
2.66	-7.32	-20.11	-0.49	3.04	-6.24	-17.09	-0.40	2.05	-2.07	-5.63	-0.13
2.07	1.51	4.11	0.11	2.59	-3.56	-9.69	-0.22	1.77	-0.88	-2.40	-0.05
1.97	3.35	9.12	0.26	2.05	-1.64	-4.47	-0.10	1.51	0.25	0.69	0.02
				1.78	0.45	1.21	0.03	1.42	0.41	1.12	0.03
				1.57	1.13	3.06	0.07				
				1.45	1.34	3.66	0.08				
				1.06	1.61	4.38	0.10				

Table A.8: Plotting data for Fig. 4.15 (a) and (b)

Fig. 4.15 (a)				Fig. 4.15 (b)			
$E-E_{pzc}$ (V)	pH 3	pH 6.5	pH 10	$E-E_{pzc}$ (V)	pH 3	pH 6.5	pH 10
	Estimated Na^+ surface charge (C/g)				Observed Na^+ surface charge (C/g)		
-1	1.33E+09	9.43E+08	9.89E+08	-1	5.35	15.23	22.83
-0.8	2.70E+07	1.91E+07	2.00E+07	-0.8	3.01	11.07	19.90
-0.6	5.47E+05	3.86E+05	4.05E+05	-0.6	1.05	8.27	11.82
-0.3	1.58E+03	1.13E+03	1.20E+03	-0.3	0.80	3.88	5.18
0	2.64E+00	2.11E+01	3.72E+01	0	0.76	0.43	-0.71

Table A.9: Plotting data for Fig. 4.16 (a) and (b)

Fig. 4.16 (a)													
-1.0V		-0.8V		-0.6V		-0.3V		0 V		0.2V		0.4 V	
pH_i	pH_f	pH_i	pH_f	pH_i	pH_f	pH_i	pH_f	pH_i	pH_f	pH_i	pH_f	pH_i	pH_f
5.81	3.37	6.36	3.61	3.19	3.14	6.5	5.5	6.35	6	3.18	3.19	3.17	2.7
3.18	3.12	3.15	3.21	10.25	3.97	10.48	9.62	3.16	3.19	6.34	10.28	6.52	10.36
9.97	3.59	10.45	3.35	10.25	3.97			10.75	10.5	10.41	10.53	10.31	11.13
10	3.5			5.75	3.75								
Fig. 4.16 (b)													
-1.0V		-0.8V		-0.6V		-0.3V		0 V		0.2V		0.4 V	
Δ pH	σ_{Na+} (C/g)	Δ pH	σ_{Na+} (C/g)	Δ pH	σ_{Na+} (C/g)	Δ pH	σ_{Na+} (C/g)	Δ pH	σ_{Na+} (C/g)	Δ pH	σ_{Na+} (C/g)	Δ pH	σ_{Na+} (C/g)
2.44	15.23	2.75	11.07	0.05	1.05	1.00	3.88	0.35	0.43	-0.01	0.17	0.47	-0.15
0.06	5.35	-0.06	3.01	6.28	12.40	0.86	5.18	-0.03	0.76	-3.94	-4.63	-3.84	-8.68
6.38	25.39	7.10	19.90	6.28	11.82			0.25	-0.71	-0.12	-2.03	-0.82	-14.53
6.50	22.83			2.00	8.27								

Table A.10: Plotting data for Fig. 4.22 (b)

Adsorption for 80 min		Adsorption for different time at -0.3V		
E (V)	σ_{Na+} (C/g)	E (V)	Time (min)	σ_{Na+} (C/g)
-0.7	15.23	-0.3	2	1.56
-0.5	11.07	-0.3	5	3.74
-0.3	7.49	-0.3	20	6.40
0	3.88	-0.3	40	7.17
0.3	0.43	-0.3	80	9.25

Table A.11: Plotting data for Fig. 4.23 (a) and (b)

Fig. 4.23 (a)				Fig. 4.23 (b)					
	Point method (-0.3V)	E_{pzc}	Area method	Point method (-0.3V)		Direct sorption 80 min		10 min	
$[NaCl]_i$ (mM)	$-C_c$ (F/g)	$-C_c$ (F/g)	$-C_c$ (F/g)	$[NaCl]_i$ (mM)	$-C_c$ (F/g)	$[NaCl]_f$ (mM)	σ_{Na+} (C/g)	$[NaCl]_f$ (mM)	σ_{Na+} (C/g)
1	4.73	1.18	0.45	1	4.73	0.06	1.57	0.10	0.59
5	10.07	4.85	2.22	5	10.07	0.50	3.94	0.53	1.18
10	15.16	9.00	4.89	10	15.16	0.61	9.26	0.81	3.23
20	19.49	14.27	8.35	20	19.49	6.99	64.87	8.84	8.96
30	22.00	18.34	10.59	30	22.00	17.76	74.62	29.48	18.67
50	25.52	23.57	13.64	50	25.52	27.38	82.00		
100	29.30	29.87	17.08	100	29.30				